# BAR-ILAN UNIVERSITY

# Photonic – Piezoelectric Circuits in Lithium Niobate

**Maayan Holsblat**

**Submitted in partial fulfillment of the requirements for the Master's Degree in the Alexander Kofkin Faculty of Engineering,**

**Bar-Ilan University**

Ramat Gan, Israel 2026

**This work was carried out under the supervision of Prof. Avi Zadok and Prof. Tomer Lewi,**
**Faculty of Engineering,**
**Bar-Ilan University**

# Acknowledgements

I would like to begin by thanking my supervisor, Prof. Avi Zadok, who took me under his wing already in the third year of my B.Sc. studies and continued to guide me throughout my M.Sc. Your support over these years, your availability for every question, and your commitment to both the scientific and personal growth of your students have shaped my path more than any course or textbook ever could. Beyond being a brilliant scientist, you are a truly caring person, and I feel privileged to have been part of your group.

My sincere thanks go to the members of the Devices Team for your mentoring, patience, and hands-on help in the lab and cleanroom: Matan Slook, Inbar Shafir, Shai Ben Ami, Leroy Dokhanian and Rafael Suna. From basic “first steps” on the tools to complex troubleshooting, you were always willing to teach, to explain one more time, and to share your experience. This thesis could not have been completed without your guidance.

I am also grateful to the rest of our research group: Shahaf Noimark, Ori Pearl, Elad Zehavi, Alon Bernstein, Guy Deutch, Elad Layush and Ohad Buch. You have been true friends as much as colleagues, and you are a major reason why I arrived at the university with a smile. The conversations, jokes, support, and the feeling of being part of a close-knit group made this period of my life meaningful and enjoyable.

I would like to thank Dr. Boris Desiatov for his invaluable help in understanding lithium niobate photonics, for the insightful discussions, and for providing devices that were essential for this work. I am deeply grateful to Dr. Mirit Hen for her continuous help with the practical and administrative aspects of the research. I am also grateful to Prof. Tomer Lewi for his support, guidance, and encouragement throughout this work.

My appreciation extends to the Faculty of Engineering at Bar-Ilan University for supporting this research, including through generous scholarship. It also extends to BINA and its cleanroom staff for providing excellent facilities and professional support. The guidance of the engineers in the cleanroom, and their patience while I learned the processes, were crucial for the fabrication and characterization stages of this project.

I would like to thank Soreq Nuclear Research Center and our friend Ohad Westreich for giving me the opportunity to take part in the measurements conducted there, and for the explanations and discussions that helped me better understand the results and their implications.

This thesis was carried out during a difficult period in which Israel was at war. I want to express my deep gratitude to all the defense and security forces who protect this country and allow us to continue studying, working, and doing research. I also wish to honor my dear friends who lost their lives during the war so that we can live here. Their memory and sacrifice are present in my thoughts as I complete this work.

To my family, and especially to my parents, I owe more than words can express. Thank you for your endless support, patience, and encouragement; for believing in me all throughout my life and for giving me the stability and love that made it possible to dedicate so much time and energy to this thesis.

Finally, I thank God for granting me life, health, and strength. I feel His guidance with me throughout my life, and I am grateful for all the blessings He has given me.

# Contents

## List of figures

## List of Acronyms

| | |
|---|---|
| **BINA** | Bar-Ilan Institute of Nanotechnology and Advanced Materials |
| **BPF** | Band Pass Filter |
| **CMOS** | Complementary Metal Oxide Semiconductor |
| **DMSO** | Dimethyl Sulfoxide |
| **EBL** | Electron-Beam Lithography |
| **EDFA** | Erbium-Doped Fiber Amplifier |
| **ER** | Extinction Ratio |
| **FSR** | Free Spectral Range |
| **FWHM** | Full Width at Half Maximum |
| **IDT** | Interdigital Transducers |
| **IPA** | Isopropanol |
| **$LiNbO_3$** | Lithium Niobate |
| **LNOI** | Lithium Niobate on Insulator |
| **LPCVD** | Low-Pressure Chemical Vapor Deposition |
| **PC** | Polarization Controller |
| **PD** | Photo Detector |
| **PIC** | Photonic Integrated Circuit |
| **PID** | Proportional-Integral-Derivative |
| **Q Factor** | Quality Factor |
| **RIU** | Refractive Index Units |
| **RF** | Radio Frequency |
| **SAW** | Surface Acoustic Wave |
| **SiN** | Silicon Nitride |
| **$SiO_2$** | Silicon Dioxide |
| **SOI** | Silicon on Insulator |
| **TE** | Transverse Electric |
| **TFLN** | Thin Film Lithium Niobate |
| **TM** | Transverse Magnetic |
| **VNA** | Vector Network Analyzer |

## List of Notations

| Notation | Units | Description |
|---|---|---|
| $c$ | $[\frac{\mathrm{m}}{\mathrm{sec}}]$ | Speed of light in vacuum |
| $f$ | [Hz] | Radio frequency |
| $H(\Omega)$ | | Radio-frequency response of a surface acoustic wave-photonic device |
| $H_G(\Omega)$ | | Frequency response of surface acoustic waves stimulation |
| $k_0$ | $[\frac{\mathrm{rad}}{\mathrm{m}}]$ | Vacuum wavenumber |
| $L_c$ | [m] | Coupling length |
| $n$ | RIU | Refractive index |
| $n_{eff}$ | RIU | Effective index |
| $n_{group}$ | RIU | Group index |
| $P$ | $[W]$ | Optical power |
| $V$ | | Parameter of optical waveguides |
| $V_\pi$ | $[V]$ | Modulator voltage swing |
| $v$ | $[\frac{\mathrm{m}}{\mathrm{sec}}]$ | Phase velocity |
| $v_g$ | $[\frac{\mathrm{m}}{\mathrm{sec}}]$ | Group velocity |
| $\Delta n$ | RIU | Change in refractive index |
| $\Delta P$ | $[W]$ | Change in optical power |
| $\Delta y$ | $[m]$ | Offset between adjacent waveguide sections |
| $\alpha$ | $[\frac{1}{m}]$ | Linear losses coefficient |
| $\beta$ | $[\frac{\mathrm{rad}}{\mathrm{m}}]$ | Propagation constant |
| $\kappa$ | $[\frac{1}{m}]$ | Coupling coefficient |
| $\lambda$ | $[m]$ | Optical wavelength |
| $\lambda_0$ | $[m]$ | Vacuum wavelength |
| $\Lambda$ | $[m]$ | Grating period |
| $\tau$ | $[sec]$ | Group delay |
| $\omega$ | $[\frac{rad}{\mathrm{sec}}]$ | Angular optical frequency |
| $\bar{E}$ | $[\frac{\mathrm{V}}{\mathrm{m}}]$ | Electric field vector |
| $\phi_{round-trip}$ | [rad] | Accumulated phase |

## Abstract

Integrated photonics is a cornerstone technology for compact optical systems in telecommunications, sensing, computing, and quantum applications. Integrated systems bring together high-quality passive waveguides layouts, modulators, detectors, and even light sources for enhanced performance and scalability. However, the implementation of certain functions in integrated photonics remains challenging. For example, analog processing of microwave signals requires long true time delays which cannot be accommodated on-chip at the speed of light. Surface acoustic waves (SAWs) offer a powerful solution: their velocity, which is orders of magnitude slower than that of light, leads to substantial delays over small footprint. In addition, photoelastic interaction with acoustic waves can induce GHz-rate modulation in key photonic integration platforms that are otherwise strictly passive, such as silicon nitride. While piezoelectric actuation provides the most efficient SAW generation, the effect is absent in silicon-on-insulator, silicon nitride, and many other significant photonics platforms.

In this work, the integration of piezoelectric and photonic circuits is explored using thin-film lithium niobate (TFLN). The study focuses on SAW photonic devices that leverage the strong piezoelectric actuation of lithium niobate to modulate optical signals through the photoelastic effect. Two approaches for SAW–photonic integration are investigated. The first uses strip-loaded waveguides on TFLN to enable extremely simple fabrication, without etching the lithium niobate layer. Inter-digitated transducers on the TFLN surface are used for the actuation of SAWs, and photonic readout is realized through photo-elastic modulation of guided light in racetrack resonator waveguides. The SAW-photonic response is characterized by resonance frequencies between 300-400 MHz, which correspond to acoustic modes of the device layers stack. The extent of induced index perturbation is estimated in the sixth decimal point.

A second set of devices used heterogeneous integration of a lithium niobate slab on top of a silicon nitride photonic circuit. The devices were designed and characterized by our group, and fabricated by the commercial foundry Ligentec, Switzerland. The devices bring together piezoelectric actuation in the lithium niobate layer, and high-quality passive photonic circuits in silicon nitride: the quality factor of resonators reached 1.5 million. Acousto-optic modulation in buried silicon nitride waveguides was demonstrated at 300 MHz frequency. The photoelastic index perturbation in the devices was estimated in the seventh decimal point, restricted by a capping layer of silica on top of the actuation electrodes. Nevertheless, the hybrid devices introduce high-rate modulation to the essential photonics platform of silicon nitride. Further studies will examine the dependence of SAW-photonic response on the crystalline orientation of the transducer electrodes, the polarization of guided light, and the choice of two buried silicon nitride core layers. Overall, this research results establish lithium niobate-based SAW-

photonics as a viable platform for acousto-optic modulation and analog microwave photonic signal processing

# 1. Introduction

## 1.1 Photonic Integrated Circuits

Optical communication systems are essential for broad bandwidth data transmission. Over the years, optical communication has gradually shifted from exclusively long-haul networks to the rack, board, and chip levels [1]. Compared with electrical connectivity, optics supports much higher data rates, covers far longer distances, and provides immunity to electromagnetic interference [2]. The large volumes of short-reach, data-center communications are the main driving force behind photonic integrated circuits (PICs). Integration of multiple photonic components, such as waveguides, modulators, detectors, and lasers, critically reduces cost, size, and power consumption. The integration of photonic components on a single chip facilitates complex optical signal processing and high-speed data transmission with improved reliability and scalability [3].

Silicon photonics has emerged as a leading platform for PICs due to its compatibility with complementary metal-oxide-semiconductor (CMOS) manufacturing processes. Silicon photonics leverages the well-established silicon fabrication infrastructure. Most importantly, silicon photonics enables the co-integration of electronic and optical functions in a system on a single chip. Silicon-based PICs are widely used in telecommunications, data centers, and emerging applications such as quantum computing and bio-photonics [3].

In addition to silicon, other materials such as lithium niobate ($LiNbO_3$) and silicon nitride (SiN) are also used in PICs for specific applications where their unique properties offer distinct advantages [4]. Lithium niobate is a non-centrosymmetric crystal, therefore it exhibits second-order nonlinearities and piezoelectricity. Of all such crystals, lithium niobate offers the most advanced PIC technology. Lithium niobate is the material of choice for electro-optic modulators in optical fiber telecommunications [5]. Its piezoelectric properties are especially useful in surface acoustic wave (SAW) devices, which convert electrical signals into mechanical vibrations and vice versa, essential for analog signal processing in mobile communications and other analog electronics [6].

Silicon nitride is a strictly passive waveguide platform. Compared with silicon, SiN provides transparency in visible and near-IR wavelengths and ultra-low propagation losses at telecommunication wavelengths [7]. It is also free of two-photon absorption which restricts the optical power handling of silicon at telecommunication wavelengths. SiN is the material of choice in many quantum technology and bio-sensing applications [8], [9].

The continuous development of PICs and the exploration of different materials are driving innovations in photonic devices, pushing the boundaries of performance and enabling new applications across various fields [10]. As the demand for high-bandwidth, low-latency, and

energy-efficient communication systems continues to grow, PICs are set to play a critical role in the future of optical technology [11].

## 1.2 Basic building blocks of passive photonic circuits

Integrated photonic circuits rely on a set of fundamental building blocks for controlling and manipulating the propagation of light. This section describes the essential structural and functional elements that form the foundation of passive photonic systems across all material platforms: optical waveguides, directional couplers, and ring resonators. While the framework is presented here in the context of silicon photonics, it is universally applicable to other integrated photonic material systems such as SiN and $LiNbO_3$. Although specific geometric implementations, material parameters, and fabrication protocols vary across material platforms, the underlying concepts remain consistent.

### Optical Waveguides

Optical waveguides form the foundational structural elements of integrated photonic circuits, serving to confine and guide electromagnetic waves of optical frequencies along pre-defined paths. Standard waveguides leverage the principle of dielectric confinement: light is restricted to a higher-refractive-index core surrounded by lower-index cladding materials. Propagation is governed by the wave equation:

$$\nabla^2\vec{E} + n^2{k_0}^2\vec{E} = 0. \tag{1.1}$$

Here, $\vec{E}$ is the frequency-dependent electric field vector, and $n$ is the spatially varying refractive index. $k_0 = \frac{\omega}{c} = \frac{2\pi}{\lambda}$ is the vacuum wave number, where $\omega$ denotes the angular frequency, $\lambda$ is the vacuum wavelength, and $c$ is the speed of light in vacuum.

Analytic solutions to the wave equation may be found for one-dimensional slab waveguides, in which the refractive index varies with the vertical $x$ coordinate only. I assume without loss of generality that light is propagating along the $\hat{\boldsymbol{z}}$ axis. The electric field vector, in that case, may be expressed as:

$$\vec{E}(x,z,\omega) = \vec{E}_T(x,\omega)e^{-j\beta(\omega)z} \tag{1.2}$$

where $\vec{E}_T(x,\omega)$ is the transverse profile of the field at frequency $\omega$, and $\beta$ is the frequency-dependent propagation constant. Substituting this solution into the general wave equation yields the one-dimensional eigenmode equation in $x$:

$$\frac{\partial^2}{\partial x^2}\vec{E}_T + [n^2(x)k_0^2 - \beta^2]\vec{E}_T = 0 \tag{1.3}$$

The solutions correspond to the allowed guided modes, each characterized by its propagation constant $\beta$.

Let us consider a core layer of thickness $d$ and refractive index $n_{core}$, surrounded by an infinite cladding of index $n_{clad} < n_{core}$ above and below. Solutions may be classified as either transverse electric (TE) or transverse magnetic (TM). In the TE case the electric field contains $\hat{\boldsymbol{y}}$ component only, and in TM modes the same holds for the magnetic field. The propagation constants of symmetric TE modes are found through solutions to the following equation, derived from the continuity requirements at the upper and lower boundary of the cladding:

$$\frac{hd}{2}\tan\left(\frac{hd}{2}\right) = \frac{qd}{2} \tag{1.4}$$

Here $h^2 = k_0^2 n_{core}^2 - \beta^2$ and $q^2 = \beta^2 - k_0^2 n_{clad}^2$. The propagation constants of anti-symmetric modes are given by the solution of a modified equation:

$$\frac{hd}{2}\cot\left(\frac{hd}{2}\right) = -\frac{qd}{2} \tag{1.5}$$

Once the propagation constant is found, the transverse profile of the electric field $E_y(x, \omega)$ is readily obtained as well. TM modes are similarly solved subject to slightly different boundary conditions. The number of modes of each type is governed by the following parameter:

$$V = \frac{\pi d}{\lambda}\sqrt{n_{core}^2 - n_{clad}^2} \tag{1.6}$$

When $V < \pi/2$, only a single TE mode and a single TM mode are guided by the device. This so-called single mode regime is highly preferable in most photonics applications, as it avoids the detrimental effects of multiple modes having different propagation constants $\beta$ (modal dispersion). Since the indices and wavelength are often fixed, the single mode regime and be reached by reducing the core thickness $d$. For silicon cores within silica and telecommunication wavelengths, the thickness is in the order of few hundreds of nm.

One-dimensional slab geometries as discussed above do not confine light in the lateral in-plane direction, and they are seldom useful in real-world devices. Most waveguide geometries therefore rely on a core of finite height and width, surrounded by lower index cladding in two dimensions. The modes of two-dimensional waveguide cross-sections cannot be solved analytically, and they require numerical methods. Here too, sufficiently small cores would support only a single mode of each type. It is even possible to achieve propagation in a single TE mode, with no TM solution at all.

We may now define the effective index of a guided mode:

$$n_{eff} = \frac{\beta}{k_0} \tag{1.7}$$

This parameter represents the apparent refractive index "seen" by the guided mode, and it depends on the material indices, waveguide cross-sectional geometry, and optical wavelength. The effective index exhibits wavelength dependence due to both material dispersion and geometric effects related to mode confinement. The wavelength dependence is quantified, to the first order, through the group index:

$$n_{group} = n_{eff} - \lambda \frac{dn_{eff}}{d\lambda}, \tag{1.8}$$

and group velocity:

$$v_g = \frac{c}{n_{group}}. \tag{1.9}$$

The group velocity governs the propagation delays of broadband pulse envelopes on top of optical carrier waves.

### Directional Couplers

Directional couplers enable controlled power transfer between adjacent optical waveguides through overlap between evanescent fields. These devices form the fundamental basis for power splitters, switches, interferometers, and resonant cavities across all integrated photonic platforms. When two waveguides are positioned in close proximity, their individual guided modes can interact through spatial overlap of the evanescent field tails extending into the surrounding medium. This coupling mechanism can be analyzed using coupled-mode theory, which treats the overall field as a superposition of the modes from the two individual waveguides:

$$\vec{E}(x,y,z,t) = A(z)\vec{E}_a^T(x,y)e^{-j\beta_a z - j\omega t} + B(z)\vec{E}_b^T(x,y)e^{-j\beta_b z - j\omega t} \tag{1.10}$$

where $\vec{E}_{a,b}^T(x,y)$ [m$^{-1}$] are the normalized transverse field profiles of the two waveguides $a$ and $b$, and $A(z)$ and $B(z)$ [Volts] are complex amplitudes that slowly varying along the propagation direction $z$.

Substituting the superposition of the two modes into the wave equation yields the coupled-mode equations that describe the evolution of the two magnitudes [12]:

$$\frac{dA}{dz} = -j\kappa_{\mathrm{ab}} B e^{j(\beta_{\mathrm{a}} - \beta_{\mathrm{b}})z} \tag{1.11}$$

$$\frac{dB}{dz} = -j\kappa_{\mathrm{ba}} A e^{-j(\beta_{\mathrm{a}} - \beta_{\mathrm{b}})z} \tag{1.12}$$

The coupling coefficients $\kappa_{\mathrm{ab}}$ and $\kappa_{\mathrm{ba}}$ quantify the strength of evanescent interaction and depend on the spatial overlap between the modal field distributions [12]. For symmetrical devices comprised of identical waveguides ($\beta_{\mathrm{a}} = \beta_{\mathrm{b}} = \beta$, the coupling coefficients are

identical ($\kappa_{ab} = \kappa_{ba} = \kappa$). With initial conditions placing all power in waveguide a ($A(0) = A_0, B(0) = 0$), the power evolution along the two waveguides is given by:

$$|A(z)|^2 = |A_0|^2 \cos^2(\kappa z) \tag{1.13}$$

$$|B(z)|^2 = |A_0|^2 \sin^2(\kappa z) \tag{1.14}$$

The solution describes periodic, oscillatory power transfer between the two waveguides. Complete power transfer from waveguide $a$ to waveguide $b$ occurs following a distance of:

$$L_c = \frac{\pi}{2\kappa}, \tag{1.15}$$

referred to as the coupling length. It is inversely proportional to the coupling coefficient and thus depends on the separation between waveguides. Smaller separations produces stronger coupling and shorter coupling lengths.

### Vertical Directional Couplers

In addition to lateral (horizontal) directional couplers between adjacent waveguides at the same layer, vertical directional couplers enable power transfer between spatially separated layers of waveguides. In vertical couplers, two waveguides are positioned with horizontal alignment yet at different layers, separated by a thin lower-index medium such as silicon dioxide. Vertical couplers follow the same principle as lateral ones: evanescent fields overlap between the modes of two separate waveguides, and they are described by the same equations. The coupling strength is heavily affected by the vertical separation: the thickness of the dielectric layer between the two waveguides. Vertical couplers are particularly useful in hybrid devices with core layers made of different materials.

### Ring Resonators

Ring resonators are closed-loop waveguide structures coupled to external bus waveguides through directional couplers. These devices exhibit sharp spectral resonances through constructive and destructive interference of light circulating repeatedly around the loop, making them powerful tools for wavelength-selective filtering and field enhancement within the cavity.

Let us denote the circumference of the closed-loop waveguide by $L$. As light propagates around the loop, it accumulates phase according to:

$$\phi_{round-trip} = \beta L = \frac{2\pi n_{eff} L}{\lambda} \tag{1.16}$$

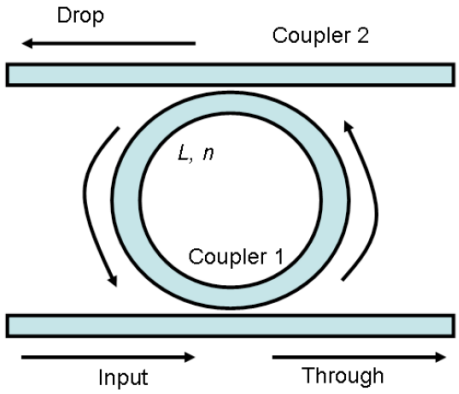


*Figure 1: Schematic illustration of a ring resonator waveguide.*

Resonance occurs at wavelengths where the round-trip phase satisfies:

$$\beta L = 2\pi m \tag{1.17}$$

where $m$ is an integer. The resonance condition is associated with periodic narrow transmission notches in the through port (see Fig. 1), accompanied by complementary transmission peaks in the drop port (if one exists). The free spectral range (FSR) of the device is defined by the wavelength spacing between two adjacent resonances:

$$FSR = \frac{\lambda^2}{n_g L} \tag{1.18}$$

The residual transmission at resonant notches depends on the splitting ratio of the directional coupler (or couplers) which form the loop. Let us consider a device with a through port only, so that the upper coupler in Fig. 1 does not exist, and let us denote the fraction of optical power that couples into the ring from the input port as $\kappa^2$. Residual resonant transmission reaches zero when:

$$\kappa^2 = e^{-\alpha L} \tag{1.19}$$

Here $\alpha$ is the losses coefficient within the loop waveguide [$m^{-1}$]. The above condition is referred to as critical coupling. It signifies that round-trip losses within the loop equal the losses due to out-coupling.

The Quality Factor ($Q$) of a resonator device quantifies the spectral sharpness of the resonance. and is defined as:

$$Q = \frac{\lambda}{\Delta\lambda} \tag{1.20}$$

Here $\Delta\lambda$ is the full width at half-maximum linewidth of the resonance transmission spectrum. Higher $Q$ factors correspond to narrower linewidths and sharper resonant features. The quality factor is related to the round-trip losses. At critical coupling we may obtain:

$$Q = \frac{\pi}{\alpha L} \tag{1.21}$$

The quality factors are restricted by bending and roughness-related scattering losses. The former term is affected by the curvature radius.

## 1.3 Lithium Niobate Devices

Traditional lithium niobate waveguides have been fabricated using ion exchange, where titanium ions are diffused into the lithium niobate substrate to increase the refractive index locally, forming a waveguide core [13]. These ion-exchanged waveguides have been widely used in modulators, switches, and frequency converters. However, the index contrast induced by ion exchange is limited, and the cores of such waveguides must be rather large: several microns in size [4]. Consequently, the electrodes of electro-optic modulators in lithium niobate are spaced far apart, and comparatively high voltages are needed to exert the necessary fields to obtain modulation. Control over the diffusion process can be challenging as well [4].

Recent advancements in thin film lithium niobate (TFLN) technology have revolutionized the fabrication and performance of lithium niobate devices. TFLN is fabricated by bonding a thin layer of lithium niobate onto a silica-on-silicon substrate, followed by thinning the lithium niobate layer to the desired thickness, typically in the range of a few hundreds of nanometers [4]. The layer stack is often referred to as lithium niobate on insulator, or LNOI.

LNOI offers several advantages over traditional bulk lithium niobate. It allows for much tighter mode confinement, enabling the fabrication of highly integrated and compact photonic devices. The enhanced confinement also leads to stronger interactions between the optical mode and the electro-optic or nonlinear properties of lithium niobate, resulting in improved device performance [4]. For example, the electrodes of electro-optic modulators can be brought closer, and their operation voltage is much reduced. The typical losses in TFLN waveguides at 1550 nm are between 0.1 and 1 dB/cm [4]. Additionally, the compatibility of TFLN with silicon photonics platforms opens up new possibilities for hybrid integration, combining the best features of both technologies [14].

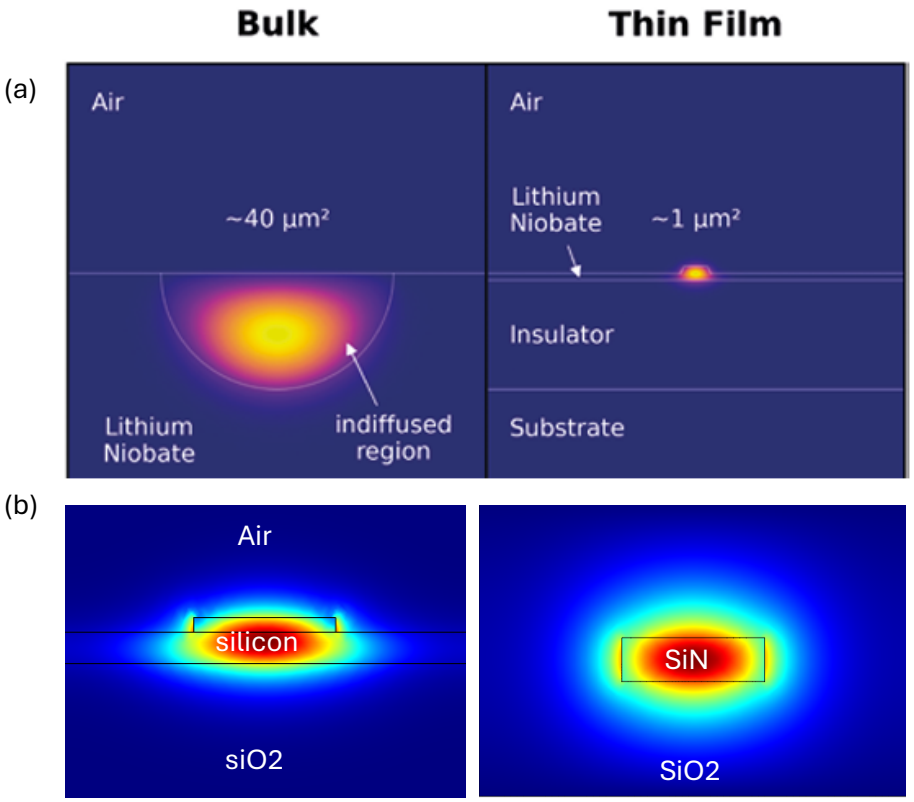


*Figure 2: (a): Cross-sections of typical waveguides for bulk (left) and thin film (right) lithium niobate [15]. (b): Calculated transverse profiles of the fundamental TE mode in a waveguide of SOI (left) and SiN (right), at a wavelength of 1550nm. The core dimensions are: SOI - unetched silicon 150 nm thick with ridge 70 nm high × 700 nm wide; SiN - 300 nm high × 1 µm wide.*

## 1.4 Silicon Nitride Photonics

Silicon nitride can be optimized in various ways to achieve high performance in photonic applications. Thin-layer waveguides, utilizing high-purity silicon nitride deposited through low-pressure chemical vapor deposition (LPCVD), can attain ultra-low propagation losses of 8–9 dB/m for a 0.5 mm bend radius and 3 dB/m for a 2 mm bend radius, with projections of 0.1 dB/m at a 7 mm bend radius [16]. This approach benefits from the precise control over film thickness and surface roughness that LPCVD provides, resulting in minimal scattering losses and enhanced stability.

Thick-layer waveguides (800 nm) fabricated using the photonic damascene reflow process exhibit unprecedentedly smooth sidewalls and tight confinement, which are essential for minimizing scattering losses. This process involves patterning a preform structure with recesses that define the waveguide, depositing silicon nitride, followed by a reflowing stage to smooth out any roughness. The result is resonator waveguides with quality factors of 5 million and propagation losses of approximately 5 dB/m. The thick core supports anomalous group velocity dispersion [7]. These attributes are crucial for applications such as high-resolution spectroscopy, narrow-linewidth lasers, and efficient frequency comb generation.

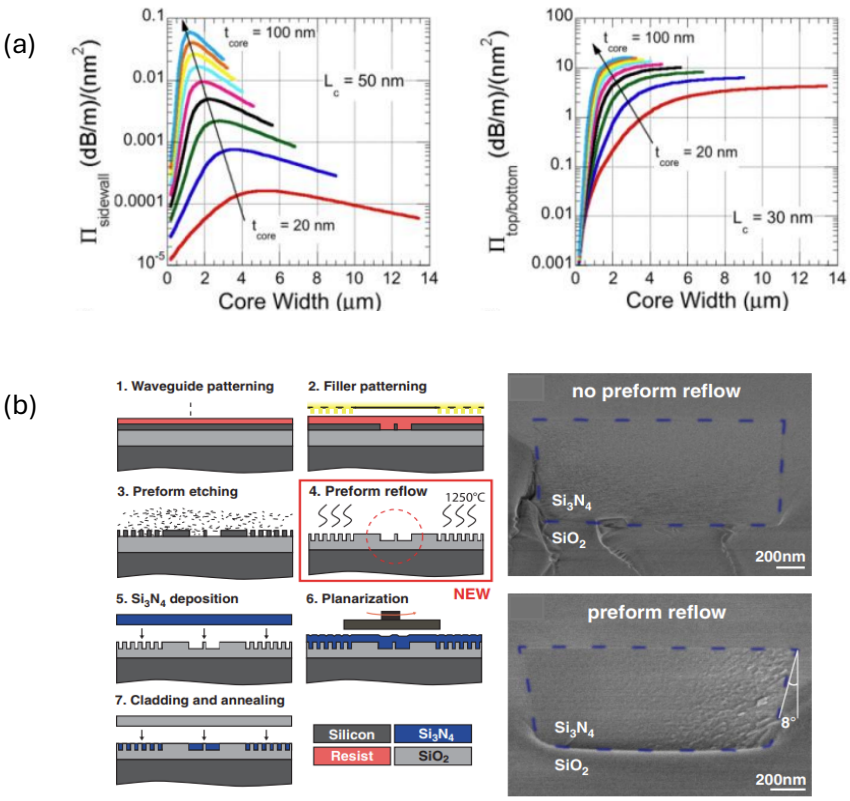


*Figure 3: (a): Simulated losses of the fundamental TE mode in silicon nitride waveguides at 1550 nm wavelength as functions of the core width, for different core thicknesses (see legend) [17]. (b): Left - Schematic flow of the photonic damascene process for fabrication of silicon nitride waveguides, highlighting the preform reflow step. Right – scanning electron microscope cross-section images of waveguides with and without reflow [7], [18].*

## 1.5 Piezoelectric Actuation of Surface Acoustic Waves, and Applications in Electronics

The piezoelectric effect refers to the generation of an electric charge in certain materials when subjected to mechanical stress. This phenomenon occurs in non-centrosymmetric crystals, such as lithium niobate, where the application of pressure or strain results in a displacement of charge centers within the material, creating an electric dipole moment [19]. This effect is reciprocal: the application of an electric field can also induce mechanical strain. The ability to convert mechanical energy into electrical energy (and vice versa) makes piezoelectric materials ideal for a wide range of applications, including sensors, actuators, and modulators in photonic and electronic devices [20].

Surface acoustic waves (SAWs) are mechanical waves that travel along the surface of a material, with their amplitude decaying exponentially with depth. SAWs can be generated through the application of an alternating electric field to a piezoelectric material, or via thermal excitation. These waves are highly sensitive to surface conditions, making them useful for detecting mass variations, pressure changes, and other surface-related phenomena [21]. The typical working principle of a SAW device involves the use of interdigital electrodes (IDTs) on

the surface of a piezoelectric material. When an alternating voltage is applied to the electrodes, a periodic electric field is created, generating a strain on the material. This strain provides the necessary boundary condition for the generation of SAWs that propagate along the surface of the material. The SAWs wavelength is determined by the spatial periodicity of the electrodes [22].

Many analog electronic filter devices rely on the launch and detection of SAWs. The realization of narrow passbands in analog filters mandates the accumulation of long group delays within the filter structure. Fast-moving electromagnetic waves cannot be delayed within small chips. In contrast, the much slower velocity of acoustic waves enables long delays within small footprints. SAW devices have been widely employed in analog electronics for 70 years [21].

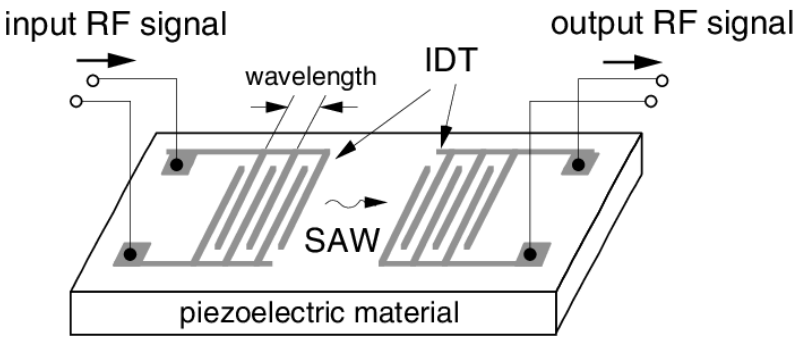


*Figure 4: SAW filter diagram. Taken from Bliley Technologies website*

## 1.6 Surface Acoustic Wave-Photonic Devices

**Piezoelectric actuation**

SAW-photonic devices carry over the benefits of acoustic waves to the realm of photonic integrated circuits. SAWs induce photoelastic perturbations to the refractive index of waveguides, leading to modulation. Similar to analog electronics, SAWs can implement long group delays within photonic circuits that cannot be implemented at the speed of light. The delays, in turn, may be used in narrowband filters. The use of SAWs helps overcome a stringent restriction: the cores of most photonic waveguides do not support acoustic modes in overlap with the optical ones [22]. SAWs, on the other hand, are anchored to the surface discontinuity of the solid substate, and they can be supported by all platforms.

Lithium niobate is a natural candidate material for SAW-photonic devices, since it is widely used in PICs and also supports piezoelectric excitation. Several works have already combined SAWs with guided light in lithium niobate. In one research, SAW resonators on lithium niobate substrates were designed and modeled. Through finite element simulations, key design parameters such as the spacing between IDTs and the number of reflectors were optimized to achieve the highest mechanical displacement and performance. This work highlights lithium niobate's high piezoelectric coupling [23]

Another study focused on phononic band structure engineering to achieve high-quality (Q) factor and small mode size SAW resonators operating at gigahertz frequencies. By using phononic crystals and adiabatically tapered structures, the researchers effectively confined phonons, resulting in Q factors exceeding 20,000 at room temperature and up to 61,000 at cryogenic temperatures. The device showcases lithium niobate's potential for high-frequency SAW applications in quantum phononics and integrated hybrid systems [24].

Most other major PIC platforms, such as silicon on insulator and silicon nitride, lack the piezoelectric excitation of acoustic waves. An alternative principle of SAW-photonic devices in these materials is presented next.

### Thermo-Elastic Excitation of Surface Acoustic Waves in Silicon Photonics

Our group has developed silicon-on-insulator (SOI) devices where SAWs are launched by thermo-elastic excitation [25], [26]. An optical pump wave illuminates a metallic grating with spatial period $\Lambda$. The intensity of the pump wave is modulated at a radio frequency $\Omega$. Absorption of light in the metals leads to periodic heating and cooling, and the associated thermo-elastic strain is transferred to the photonic circuit layers below. If the frequency $\Omega$ and wavelength $\Lambda$ of the strain pattern match those of a surface acoustic mode of the layer stack, SAWs are generated and propagate away from the grating area. The strength of these SAWs is proportional to the modulation of the pump wave's intensity [25].

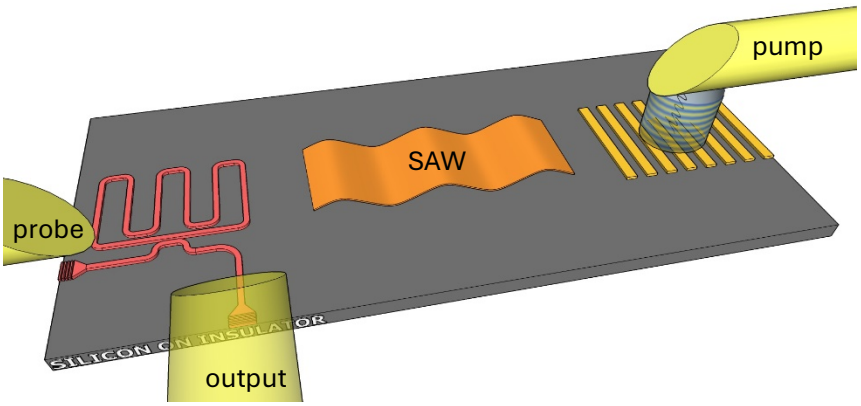


*Figure 5: A SAW-photonic device on silicon-on-insulator [27]. An optical pump wave, modulated at radio frequency Ω, illuminates a metallic grating with period Λ. Thermo-elastic expansion and contraction of the grating elements lead to the launch of SAWs. The acoustic waves pass across a photonic resonator waveguide and induce photoelastic index perturbation. These perturbations, in turn, modulate the output intensity of a probe wave in the resonator. The modulation information is transferred from pump to probe via slow moving SAWs and may acquire long delays.*

A resonator waveguide is defined in the silicon device layer near the metallic grating. The resonator consists of $N$ straight sections parallel to the grating stripes. As the SAWs propagate, they induce periodic changes in the refractive index of the waveguide sections. These changes result from the photoelastic effect, where the traveling SAWs modulate the refractive index in a time-dependent manner. A continuous probe wave is coupled into the resonator waveguide

through a second input port. The SAW-induced photoelastic index changes imprint phase modulation on the probe. The wavelength of the probe is aligned with a spectral slope of the transfer function of optical power through the resonator. With that choice, the phase modulation is converted to intensity modulation of the probe at the resonator output. Altogether, the radio-frequency modulation information is converted from the input pump to the output probe through the SAWs. The slow velocity of sound waves enables the accumulation of long temporal delays in the process.

To quantify this process, the overall transfer function between the input voltage modulating the pump wave and that of the detected output probe wave can be expressed as:

$$H(\Omega) = CH_G(\Omega) \sum_{l=0}^{N-1} a_l exp\left(-\frac{l\alpha_{SAW}\Delta y}{2}\right) exp(-jl\Omega\tau) \qquad (1.22)$$

Here $\Delta y$ is the acoustic path length between adjacent straight sections of the resonator layout, $\tau$ denotes the acoustic group delay over path $\Delta y$, $\alpha_{SAW}$ is the coefficient of acoustic intensity losses per unit length, and $a_l$ represents the complex magnitude of photo-elastic modulation in waveguide section $l = 0 \dots (N-1)$. The coefficient $a_l$ can be adjusted through the width and offset of the waveguide section. Also in the Equation, $H_G(\Omega)$ is the frequency response of thermo-elastic actuation at the grating element. It is maximal at frequency at $\Omega_{max} = v/\Lambda$, where $v$ is the phase velocity of the surface acoustic mode. The width of $H_G(\Omega)$ is approximately $\Omega_{max}/M$, with $M$ the number of periods in the grating. Lastly, $C$ is a constant factor which is determined by the power levels of pump and probe, the quality factor of the resonator, thermo-elastic and photo-elastic parameters of the layer stack, and properties of the detector and modulator used. Other than $H_G(\Omega)$, the response of the device is that of a delay-and-sum filter of multiple weighted replicas of the input [28].

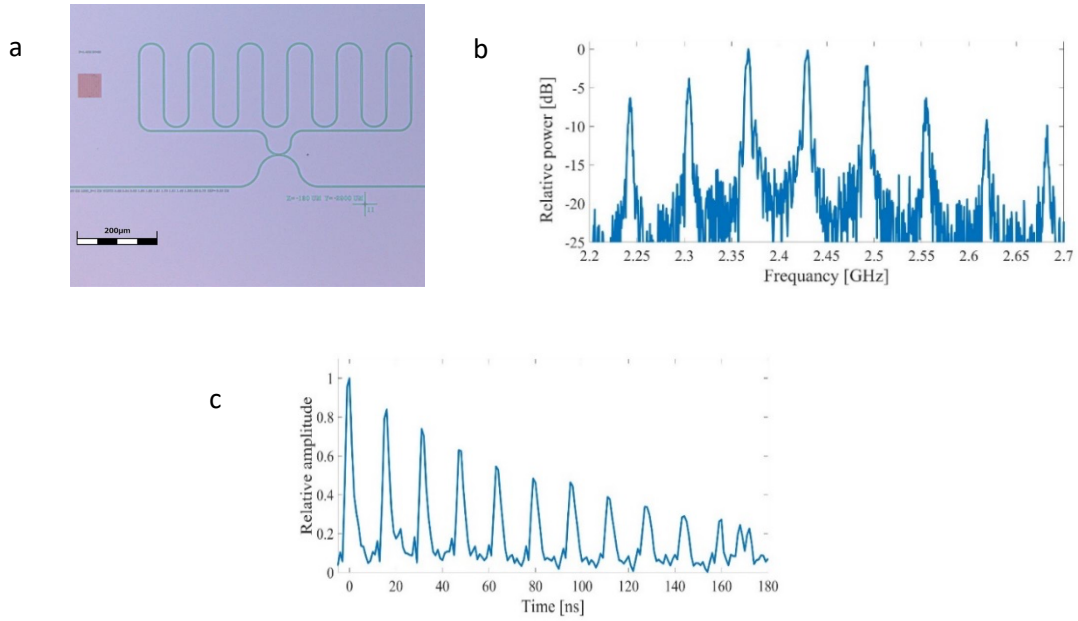


*Figure 6: (a): Top-view optical microscope image of a SAW-photonic device in SOI. The resonator waveguide consists of 12 parallel waveguide sections, implementing a radio frequency response of a 12-tap, delay-and-sum microwave-photonic filter. The scale bar corresponds to 200 μm. (b): Measured normalized transfer function of radio frequency electrical power between the modulation voltage of the input pump wave and that of the detected output probe wave. The transfer function is characterized by periodic passbands of 5 MHz bandwidth and a free spectral range of 65 MHz. (c): Measured time-domain impulse response of the same device. The response consists of 12 decaying impulses with a unit delay of 16 ns.*

Figure 6 shows a top-view optical microscope image of a SAW-photonic device, in which the resonator waveguide is designed to accumulate 12 replicas of the input waveform over 12 parallel waveguide section stretches. The transfer function of radio-frequency electrical power through the filter device consists of periodic passbands with full widths at half maximum of 5 MHz. The filter includes acoustic group delays of 175 ns over a path length of only 660 μm.

## 1.7 Waveguides Based on Strip-Loading of Slabs

The definition of waveguides in thin film lithium niobate requires etching of the layer. The process is comparatively complex and may result in losses due to surface roughness. As part of the proposed program, I also explore an alternative paradigm for the guiding of light in the lithium niobate thin layer. Instead of etching the layer, a strip of polymer may be defined on top of it. The index contrast between the strip and the air to its sides can guide an optical mode, similar to partially etched ridge waveguides. Compared with etching of the lithium niobate layer, the fabrication of strip loaded devices is simpler.

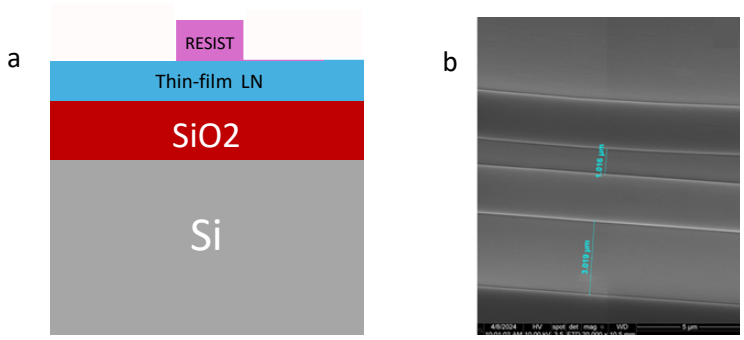


*Figure 7 :(a): Schematic illustration of the strip-loaded device with ZEP polymer on top of LNOI. (b): Top-view scanning electron microscope image of a fabricated device. The scale bar corresponds to 5 µm [Image curtsy of Dr. Boris Desiatov].*

In a recently reported work [29], a SAW-photonic device has been demonstrated in a strip-loaded TFLN device. Acoustic waves were launched through the application of voltage to interdigital electrodes on top of the lithium niobate layer. The acoustic waves then induced photoelastic modulation to probe light guided in ring resonator devices, defined by strip loading. The devices were utilized as microwave photonic filters, similar to thermo-elastic based demonstrations by our group [25], [26], operating at center frequencies of 0.78 GHz and 1.6 GHz. In my research, I follow similar strategy for realizing acoustic wave-photonic devices in TFLN. Results are reported in Chapter 3.

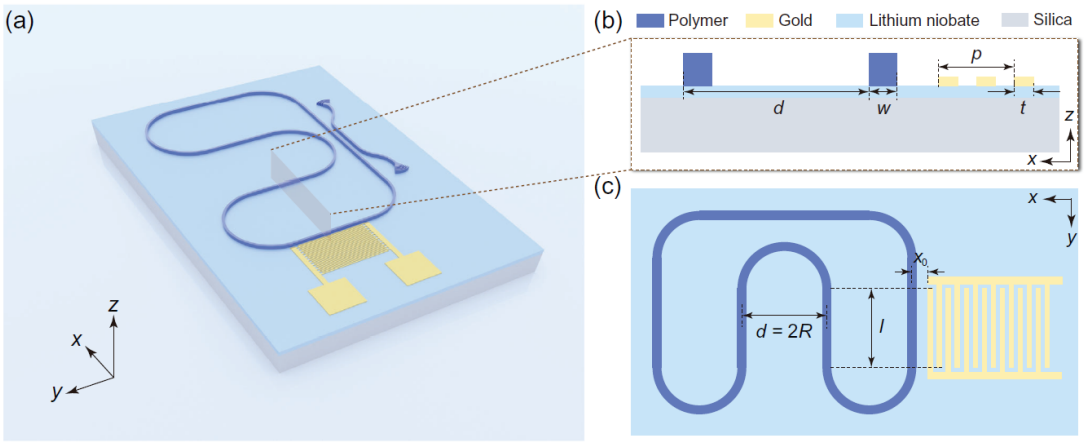


*Figure 8:(a) Illustration of a surface acoustic microwave photonic filter on an etch-less LNOI platform [29]. (b) Cross-sectional view of the acousto-optic modulation region near the IDT, with polymer waveguide (dark blue), gold IDT (yellow), lithium niobate layer (light blue), and buried silicon oxide (gray). w, d, p, and t denote the polymer waveguide width, distance between adjacent taps, IDT period, and IDT finger width, respectively. (c) Top view of the photonic microcavity and IDT, where $x_0$, d, and l denote the distance between the IDT and first tap, distance between adjacent taps, and IDT aperture, respectively.*

## 1.8 Integration of Silicon Nitride and Lithium Niobate

The integration of silicon nitride and lithium niobate holds great promise for combining the best of both platforms: CMOS-compatibility, low losses, and broad transparency of silicon nitride with the active and nonlinear functions of $LiNbO_3$. One significant work utilized wafer-scale bonding to achieve a high-yield, low-loss photonic platform. In this approach, thin-film $LiNbO_3$ was directly bonded onto $Si_3N_4$ photonic integrated circuits. This platform maintained

the low propagation losses (<0.1 dB/cm) of $Si_3N_4$ waveguides and mode converters with losses below 0.1 dB. The study showed resonators with quality factors of up to $Q = 3 \cdot 10^6$ for single resonators and up to $Q = 4.5 \cdot 10^6$ for resonator pairs, corresponding to linear propagation losses of approximately 8.5 dB/m [30]. In another demonstration of vertical hybrid integration, tapered structures at the transition regions between the two waveguide materials lowered the coupling losses to only 0.4-0.9 dB [31].

A high-performance electro-optic modulator was developed by heterogeneously integrating $LiNbO_3$ with a $Si_3N_4$ platform. The design employed an evanescent coupling structure with mode transition losses of only 0.4 dB. The Mach–Zehnder modulator fabricated on this platform achieved a half-wave voltage of 4.3 V and a modulation bandwidth of 37 GHz. The study also demonstrated successful data transmission at rates of up to 128 Gbps, underlining the practical feasibility of integrating $LiNbO_3$ on $Si_3N_4$ for high-speed optical systems [32].

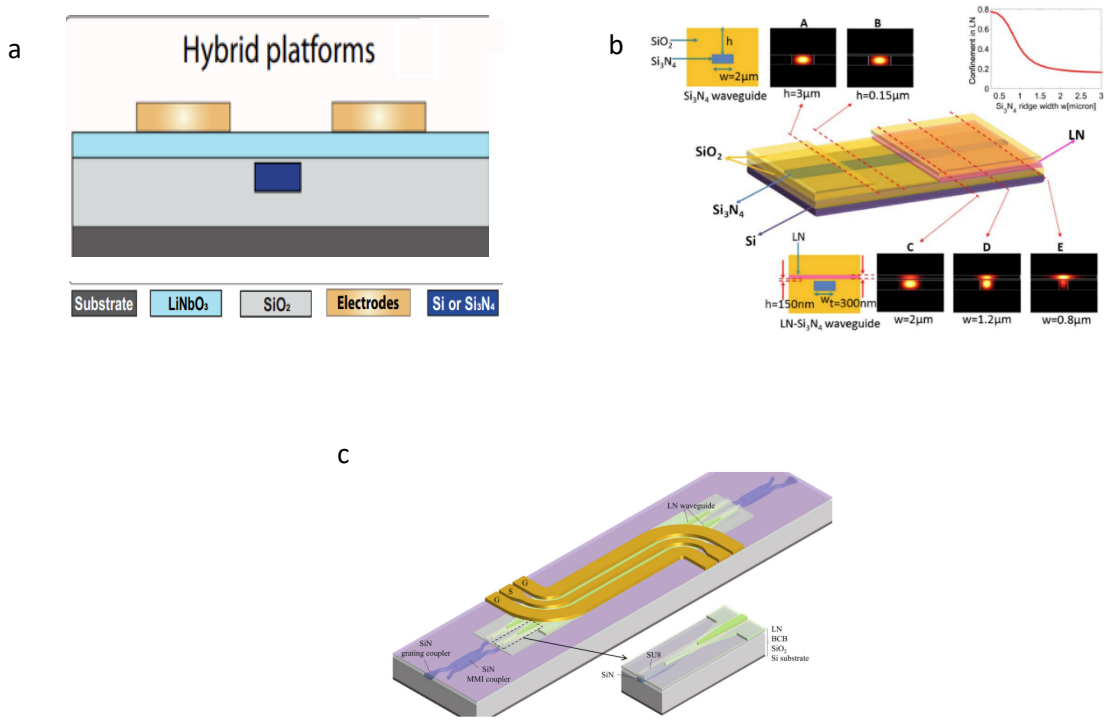


*Figure 9: Illustrations of hybrid lithium niobate – silicon nitride photonics. (a) Wafer-scale bonding of thin-film lithium niobate onto patterned silicon nitride photonic integrated circuits for scalable, low-loss platforms [30]. (b) Tapered mode converter enabling low-loss transitions between lithium niobate and silicon nitride waveguides for enhanced nonlinear photonics [31]. (c) High-performance electro-optic modulator utilizing a hybrid platform [32].*

Several works demonstrated piezoelectric actuation on top of SiN waveguides, using different material stacks. In a recent work [33], SAWs were launched through the application of voltage to interdigital electrodes on a piezoelectric slab of aluminum nitride. The SAWs induced photoelastic modulation of a probe wave in an underlying SiN waveguide. The waveguide was folded over to obtain an overall interaction length of 26 cm between the traveling SAW front

and guided light. Phase modulation was converted to an intensity reading off-chip. The actuation of multiple acoustic modes has been demonstrated, with frequencies ranging between 400-700 MHz. Modulation depth of $\pi$ radians was achieved with 10 Volts drive. Aluminum nitride was also used to launch bulk acoustic waves in a silicon nitride photonic circuit [33]. Acoustic reflections from the top and bottom surfaces of the substrate created standing waves that modulated waveguide ring resonators. In another work [34], a lead zirconate titanate (PZT) piezoelectric transducer was used to modulate an underlying silicon nitride ring resonator.

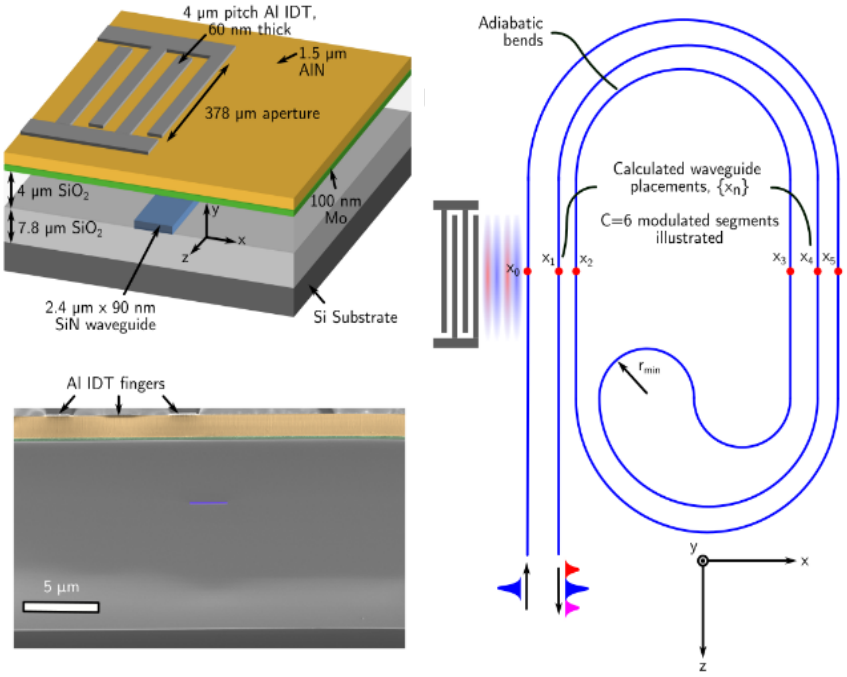


*Figure 10: An acousto-optic modulator in a hybrid layer stack [33]. Top left: schematic layout. Electrodes are deposited on top of an aluminum nitride slab. Surface acoustic waves are launched through piezoelectric exciation, and they induce photoelastic modulation of probe light guided in an underlying silicon nitride core. The core is embedded within a cladding of silicon dioxide. Bottom left :Scanning electron microscope cross-section image of a fabricated device. Right : Schematic illustration of a spiral silcion nitride waveguide adjacent to a piezoelectric actuator.*

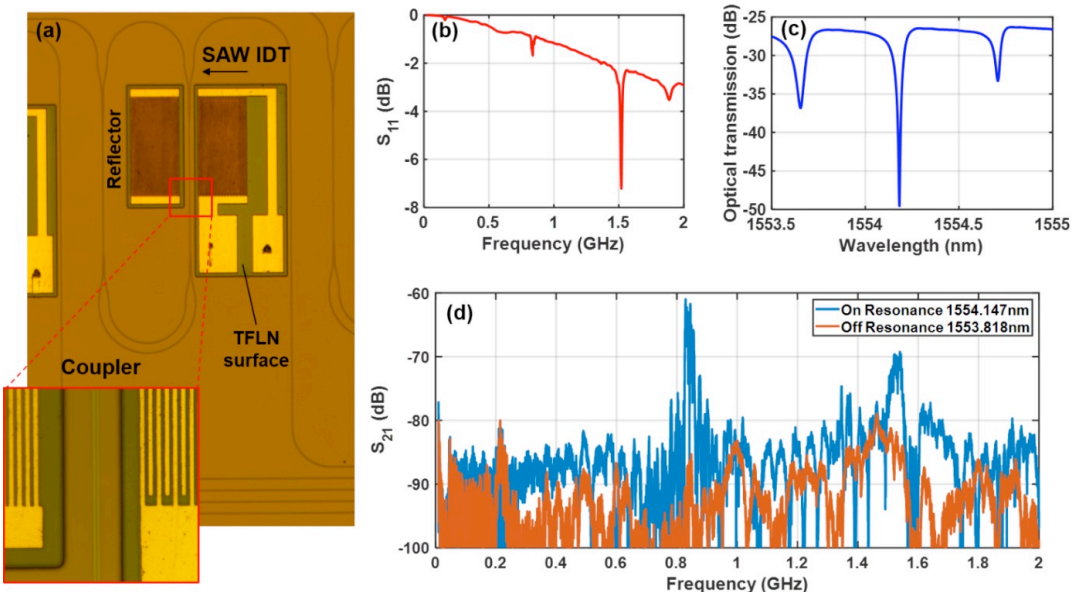


*Figure 11: (a) Optical microscope image of a fabricated hybrid SAW-photonic device, comprised of a lithium niobate slab bonded on top of a silicon nitride circuit [35]. The inset shows coupling region between input transducer and reflectors surrounding the directional coupler forming an optical racetrack resonator in the silicon nitride layer. (b) Measured radio frequency reflectivity spectrum of the interdigital electrode. (c) Measured transmission spectrum of optical power through the racetrack resonator. (d) Acousto-optic modulation response vs. frequency with the probe wavelength chosen off resonance (red) or on resonance (blue).*

To the best of our knowledge, only a single conference paper reported acoustic wave-photonic devices in a hybrid layer stack of $LiNbO_3$ on top of silicon nitride. In [35], SAWs launched from a bonded overlaying slab of $LiNbO_3$ were used to perturb the coupler region of an underlying silicon nitride resonator waveguide (Fig. 11). Comparatively weak modulation of the output probe wave has been observed. Only 100 nm of silicon dioxide separated between the silicon nitride core and the $LiNbO_3$ slab, hence the optical mode was in large overlap with the $LiNbO_3$ layer. Such proximity is not mandatory for photoelastic modulation, as demonstrated in [36] and elsewhere.

As part of this research, SAW-photonic devices were fabricated according to our design in a TFLN-SiN multi-project wafer by the Swiss foundry Ligentec. The devices include two levels of silicon waveguide cores and two orientations of the electrodes with respect to the crystalline axis of lithium niobate. Initial characterization of the newly obtained devices is presented in Chapter 4.

## 2. Objectives

The main objective of this research was to implement SAW- photonic devices that exploit the strong piezoelectric actuation of TFLN. Two implementation paths were explored:

1. SAW-photonic devices in TFLN circuits, where the optical readout waveguides and resonators are defined by the strip-loading geometry. These devices were fabricated in-house at the Bar-Ilan Institute of Nanotechnology and Advanced Materials (BINA).

2. SAW-photonic devices in Hybrid TFLN-on-silicon-nitride platform fabricated by Ligentec according to our design. In this platform, SAWs are generated in the lithium niobate layer, and the photoelastic readout is performed by ultra-low-loss, high-Q SiN resonator waveguides.

The outcomes of the research extend the state of the art in SAW-photonics over $LiNBO_3$, introduce high-frequency active modulation functionalities to silicon nitride photonics, and demonstrate a new application of the exciting platform of TFLN-on-SiN.

## 3. Surface acoustic wave – photonic devices in strip loaded thin film lithium niobate.

### 3.1 Design of strip-loaded waveguides.

Strip-loaded waveguides in thin-film lithium niobate were designed and simulated based on two fabrication protocol options. The first possibility relies on a positive ZEP resist, in which lithographically exposed regions are washed off during development. The second alternative involves ma-N 2400 negative resist, which is washed away except for the irradiated domains. The thickness of the $LiNbO_3$ slab was 300 nm, located on top of a lower silicon dioxide cladding. The thickness of the lower cladding was taken to be infinite. Positive resist strips were 2.1 μm wide and 400 nm thick, with a refractive index of 1.543 RIU. Figure 12(a) shows the calculated normalized profile of the electric field in the TE mode of the waveguide, at 1550 nm wavelength. The effective index of the mode is 1.776 RIU. The refractive index of the negative resist is 1.606 RIU, its width was 2.1 μm and its thickness was 500 nm. The calculated effective index of the TE mode in that case was 1.787 RIU. The two options therefore lead to strip loaded waveguides of similar properties.

The surface acoustic modes of the device layer stack were numerically calculated as well, using COMSOL Multi-Physics. Figure 12(b) shows the calculated displacement profile of a surface acoustic mode in the devices layer stack. The acoustic wavelength was chosen as 11 μm, to match one of the periods chosen for fabricated electrodes. The acoustic frequency of the calculated mode with that wavelength is 388 MHz.

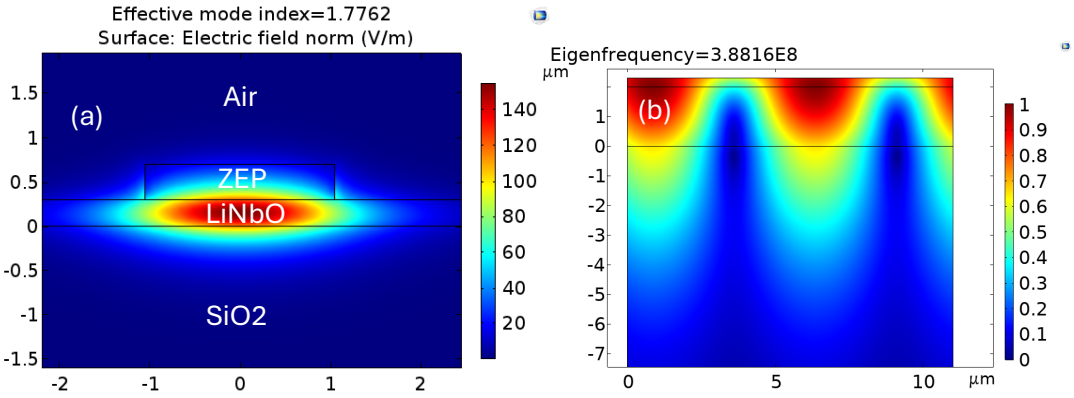


*Figure 12: Calculated transverse profiles: (a) fundamental TE mode in a $LiNbO_3$ slab with positive ZEP resist loading strip at vacuum wavelength 1550 nm. (b) fundamental acoustic mode at 388 MHz (wavelength of 11 µm) in the layer stack (top to bottom: 300 nm $LiNbO_3$, 2 µm silica, 30 µm silicon).*

## 3.2 Fabrication of a strip loaded slab of lithium niobate.

Strip-loaded devices were fabricated at the cleanroom facilities of the Bar-Ilan Institute of Nanotechnology and Advanced Materials (BINA). The process begins with a 4-inch LNOI wafer from NanoLN, which includes a lithium niobate device layer and a buried oxide layer with thicknesses of 300 nm and 2 µm, respectively. The wafer is diced to 1×1 cm² size dies. The dies are initially cleaned by immersion in dimethyl sulfoxide (DMSO) within an ultrasonic bath operating at 80 kHz frequency and 70% power for 3 minutes. The surface is then manually cleaned with swabs, and any solvent residues are rinsed off with acetone. Subsequently, the sample undergoes sonication in acetone and isopropanol (IPA) for 3 minutes each, following the same protocol.

A positive resist-based process was initially employed. To enhance the adhesion of the electron-beam resist, the sample surface was activated in a DINER oxygen plasma etcher for 5 minutes at 50% power. Following that, a positive electron beam resist (ZEP-520A) was spin-coated onto the sample. The spinning rate was 500 RPM for 5 seconds, followed by 4000 RPM for 60 seconds. The resist was baked on a hot plate at 180 °C for 3 minutes. The electron-beam lithography files, generated from the target waveguide designs using Python code, were corrected for proximity effects with Beamfox© software to prevent lithographic pattern errors. Waveguides were patterned in the resist layer using electron-beam lithography (EBL) in an ELIONIX ELS-100kV instrument, with a dose of 290 µC/cm², 1 nA beam current, and a field size of 250 µm². The resist was developed using ZED-N50 developer for 35 seconds, followed by immersion in IPA to stop the development process. The waveguides were then ready for testing.

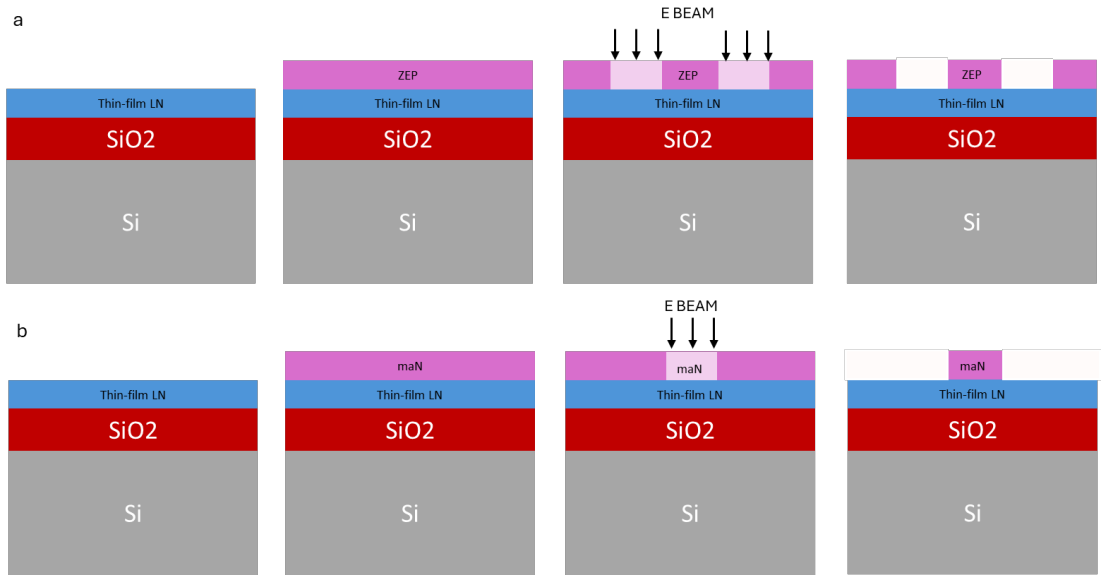


*Figure 13: Illustration of the fabrication process of strip-loaded waveguide devices on a slab of lithium niobate. (a) Positive resist: unexposed regions act as an etch mask. (b) Negative resist: exposed regions remain as resist, leaving lithium niobate open for metal deposition.*

The use of positive resists brings a significant drawback: regions away from the waveguide, where electrodes are later deposited, remain covered with resist unless they are exposed themselves. The preparation of the electrodes areas therefore requires prolonged lithography of large regions. To work around that difficulty, a negative resist was used instead. The sample surface was activated in a DINER oxygen plasma etcher for 5 minutes at 50% power. A negative ma-N 2400 electron beam resist was spin-coated onto the sample, at 3000 RPM for 60 seconds, followed by baking on a hot plate at 90 °C for 5 minutes. The pattern was written using EBL with a dose of 290 μC/cm². After exposure, the resist was developed using AZ-726 for approximately 40 seconds, followed by rinsing in DI-water and hard-baking on a hot plate at 120 °C for 1 minute. Figure 13 illustrates the fabrication steps of both methods.

The coupling of light to/from standard single-mode fibers to waveguides under test takes place through vertical grating couplers. The grating period Λ is given by:

$$\Lambda = \frac{\lambda_0}{n_{eff} - n_a \cdot \sin(\theta)} \tag{3.1}$$

Here $n_a = 1$ is the refractive index of air above the waveguide, $\theta$ is the angle of incidence with respect to the normal direction to the device substrate, and $\lambda_0 = 1550$ nm is the vacuum wavelength. Several versions of grating couplers were fabricated and tested, sweeping over the period about the nominal value of $\Lambda = 967$ nm and the grating duty cycle. For positive resist waveguides, the best performance was obtained for a 50:50 duty cycle with period $\Lambda = 977$ nm. With those parameters, coupling losses were 11 dB per interface. The minimum coupling losses to negative resist waveguides were similar, obtained with a duty cycle of 40:60 and 960 nm

period. While the coupling losses are rather high, they were sufficient for the characterization of SAW-photonic devices.

Next, ring resonators with a bending radius of 300 µm were fabricated. The transverse gap between the bus and ring waveguides in the directional coupler which forms the resonator was scanned over several values. The gap which yielded the largest extinction ratio in the transfer of optical power through the resonator was chosen for subsequent devices. A rather extensive sweep of positive resist waveguides resulted in an optimum gap of 1200 nm. The extinction ratio was 14.4 dB (Fig. 14(a) and (b)). The Q factor of the resonators was 170,000 and the FSR was 0.581 nm. Negative resist devices were only tested for two gap values of 1100 nm and 1200 nm and were not optimized further. The extinction ratio of the 1100 nm gap devices was 5 dB, sufficient for SAW photonic characterization. The Q factor was 35,500 and the FSR was 0.237nm (Fig. 13 (c) and (d)). The smaller FSR for the negative resist devices reflects their longer effective cavity length $L$: positive resist rings had $L = 1.885$ mm (pure ring geometry), while negative resist racetracks extended $L = 4.63$ mm.

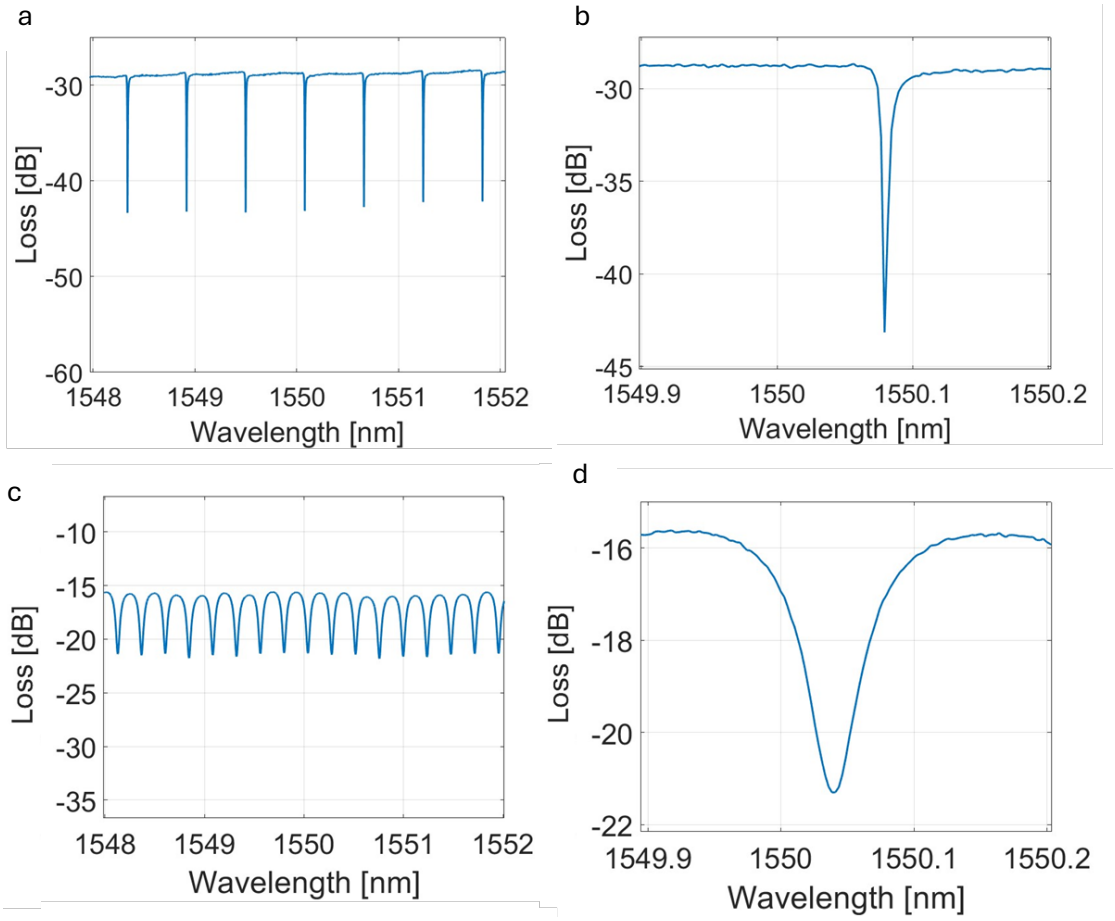


*Figure 14 : Optical vector network analyzer measurements of optical power transfer as functions of wavelength in strip-loaded ring resonators. (a): Positive resist device. (b): Magnified view of panel (a), showing one resonance transmission notch. The extinction ratio is 14.4 dB, the Q factor is 170,000 and the FSR is 0.5815 nm (c): Negative resist device. (d) Magnified view of panel (c), showing one resonance transmission notch. The extinction ratio is 5 dB, the Q factor is 35,000 and the FSR is 0.237 nm.*

## 3.3 Design and fabrication of inter-digital electrodes.

Interdigital electrodes (IDTs) were also fabricated at BINA. As an initial stage, IDTs were patterned on bulk $LiNbO_3$ substrates in order to optimize the geometry and operating frequency through wide parameter sweeps. Once a suitable set of parameters was identified, the same process was implemented on TFLN dies for integration with the strip-loaded waveguides. The fabrication process starts with spin-coating AZ-1505 positive photoresist at 4000 rpm for 60 s, followed by a soft bake on a hot plate at 100°C for 1 minute. The IDT pattern was then exposed using a maskless lithography system and developed in AZ-351 developer diluted 1:4 in deionized water for 60 s. Development was stopped by deionized water. Following development, a metal stack consisting of 5 nm Cr and 250 nm Au was sputtered to form the IDT electrodes. The thin Cr layer served as an adhesion layer between the gold electrodes and the $LiNbO_3$ surface. Lift-off in DMSO resulted well-defined Cr/Au IDT electrodes on the substrate. Figure 15 illustrates the fabrication steps

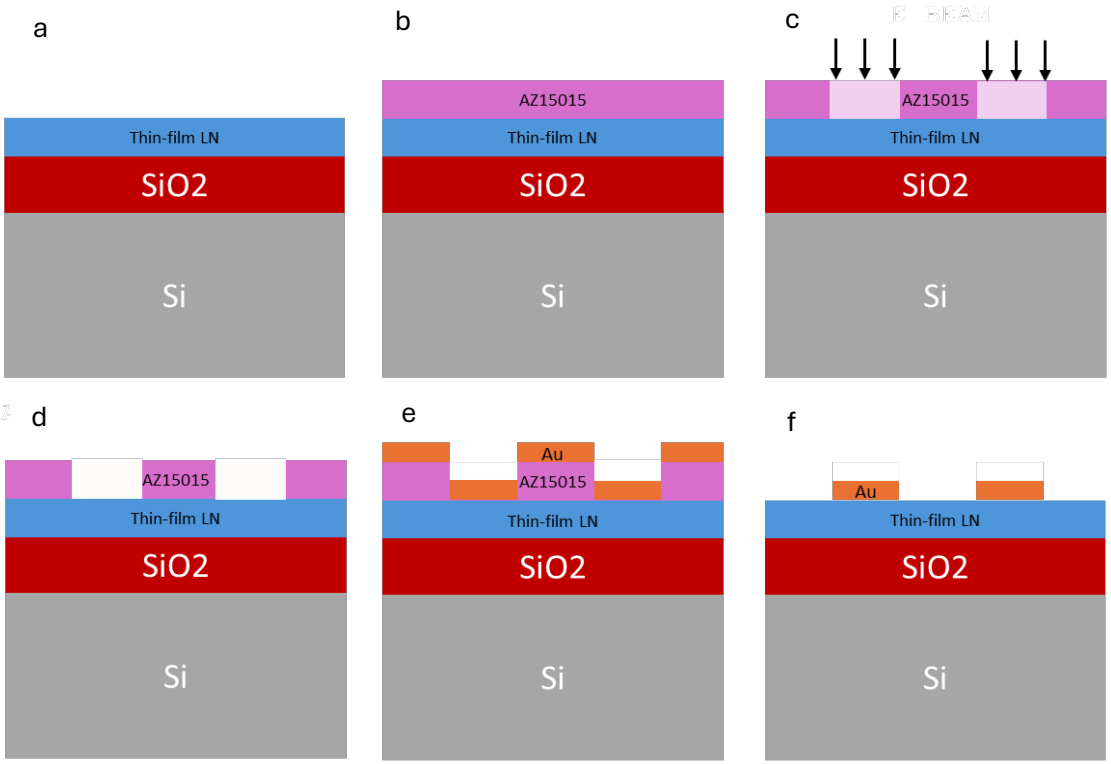


*Figure 15: Illustration of the fabrication process of inter-digital electrodes*

The IDTs comprised of 15 finger pairs (30 fingers in total). They were initially fabricated with periods $\Lambda$ between 8 and 12 µm and duty cycles between 0.4 and 0.6. Following initial characterization, two parameter combinations were chosen for integration alongside strip-loaded waveguides: Period $\Lambda = 10$ µm with 0.4 duty cycle, and $\Lambda = 11$ µm with 0.55 duty cycle. Two finger lengths were tested: 100 µm and 1 mm, and the longer option was eventually preferred. Electrodes were patterned along both the $\hat{\boldsymbol{y}}$ and the $\hat{\boldsymbol{z}}$ axes of the $\hat{\boldsymbol{x}}$-cut $LiNBO_3$, to

enable comparison between directions of propagation. A top-view microscope image of an IDT array is shown in Fig. 16.

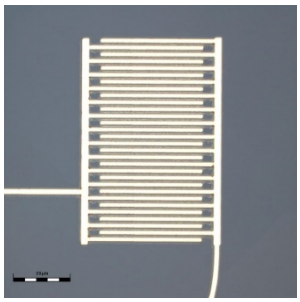

*Figure 16: Top-view optical microscope image of a fabricated array of inter-digital electrodes on bulk lithium niobate.*

## 3.4 Design and fabrication of surface acoustic wave – photonic devices

Complete devices were fabricated in two steps, using the above protocols. The IDTs were fabricated first, followed by the patterning of loading strips in negative resist with proper alignment. Some devices included two IDTs on both sides of the photonic waveguide, to enable piezoelectric detection of SAWs as well as their actuation. In those samples, a comparison between photonic and piezoelectric readout could be made. Other devices included only a single array of ITDs, for piezoelectric actuation and photonic detection only. The two above combinations of IDT periods and duty cycles were implemented. In addition, the gap between bus and ring waveguides in the strip-loading resonator layout was varied between 1100 nm and 1200 nm to maximize the extinction ratio of the optical power transfer function. Part of the layout file is presented in Fig. 17, and microscope images of devices are shown in Fig. 18.

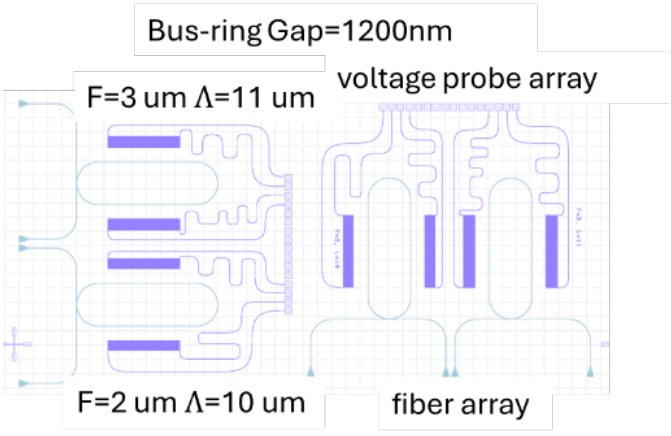


*Figure 17: Part of the layout file for the fabrication of a surface acoustic wave – photonic device in a strip-loaded thin film lithium niobate circuit. IDTs are designed in parallel with two crystalline orientations. Devices replicas differ in the IDTs periods and duty cycles. Vertical grating couplers serve for single-mode optical fibers array interface. Metallic pads at the upper right side enable the application of radio-frequency voltage to IDTs.*

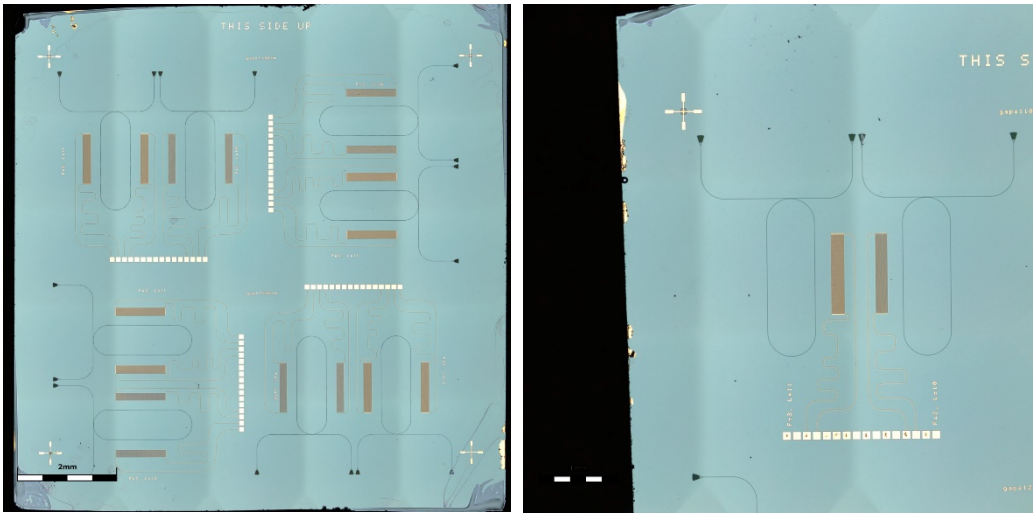


*Figure 18: Top-view optical microscope images of surface acoustic wave-photonic devices in a strip-loaded thin-film lithium niobate circuit. (left) Overview of an entire device. In this example, two IDT arrays are patterned to the sides of each photonic resonator waveguide, to enable piezoelectric actuation and detection of acoustic waves. (right) Magnified view of part of a different device, in which only a single IDT array serves for actuation. Only photoelastic detection of surface waves is supported in this device.*

## 3.5 Experimental setup

The experimental setup for the characterization of SAW devices is based on a radio-frequency vector network analyzer (VNA), connected to the on-chip IDTs via a voltage probe array. The VNA supplies the radio frequency drive signal to the transmitting IDT and simultaneously records the returned signal from the receiving port. The setup was first used in piezoelectric characterization of SAW devices between a pair of IDTs, with no photonics. In that stage, both IDTs were contacted through the voltage probe array.

In later stages, the measurements were extended to photonic readout. To that end, continuous-wave probe light from a laser diode at 1550 nm wavelength was amplified by an erbium doped fiber amplifier to 27 mW power and coupled into the bus waveguide of a resonator. One array of IDTs was driven by radio frequency signals of 0 dBm electrical power from the VNA output port. The exact probe wavelength was aligned with a spectral slope of a resonator transfer function, so the SAW-induced phase modulation was converted into intensity modulation at the resonator output. The output probe was re-amplified to 3 mW power by a second fiber amplifier and passed through an optical bandpass filter to reduce amplified spontaneous emission noise. Lastly, a broadband photoreceiver detected the output probe wave, and its electrical output was routed back to the VNA for transfer function measurements.

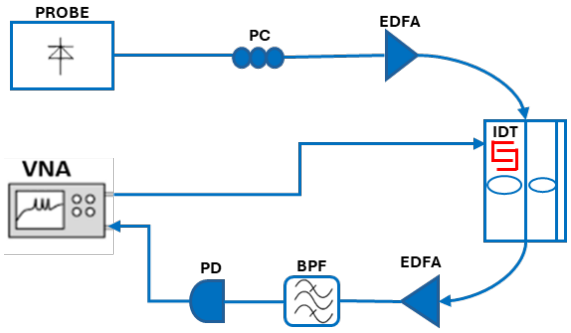


*Figure 19: Schematic illustration of the measurement setup. PC: polarization controller. BPF: band pass filter. EDFA: erbium-doped fiber amplifier. PD: photo detector. VNA: vector network analyzer*

## 3.6 Radio-frequency response of surface acoustic wave-photonic devices.

Figure 20 shows measured transfer functions of radio-frequency electrical power between two IDT arrays on bulk $LiNbO_3$. Panel (a) compares between two devices with period $\Lambda = 10$ µm and fingers width of 2 µm (duty cycle 0.4), with electrodes lengths of 100 µm and 1 mm. The electrodes were aligned with the $\hat{\boldsymbol{z}}$ axis, where resonant transmission via SAW actuation and detection occurs at 335 MHz. These results demonstrate that longer IDTs (1 mm aperture) excite stronger SAWs than shorter ones (100 µm).

Panel (b) compares between two crystallin alignments of the IDTs, with 11 µm period and 3 µm-wide fingers. Here the SAWs frequency is 313 MHz, which is lower than that in panel (a) due to the shorter acoustic wavelength. Ultimately, alignment of the electrodes along the $\hat{\boldsymbol{y}}$ axis results in signals that are more than twice larger than $\hat{\boldsymbol{z}}$ axis excitation, illustrating the anisotropy of $LiNbO_3$.

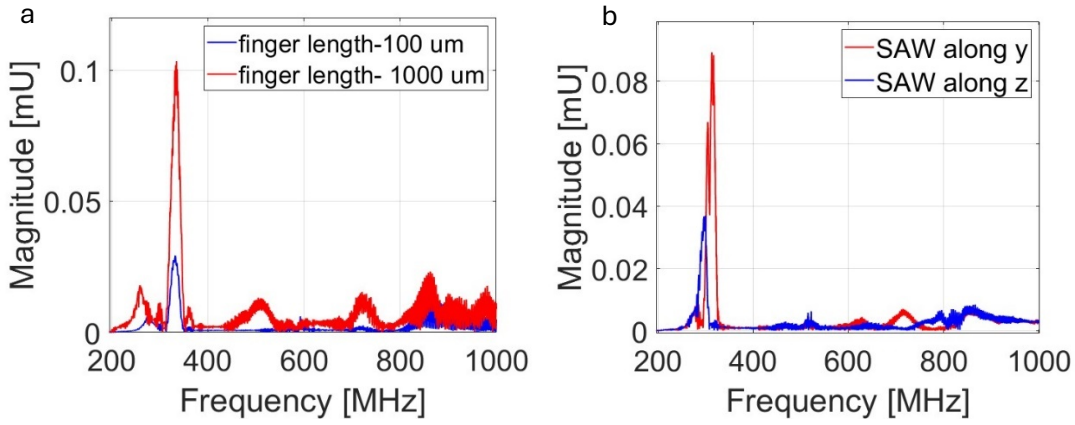


*Figure 20: Measured transfer functions of voltage vs. radio frequency between a pair of IDT arrays on bulk lithium niobate. (a): Electrodes period $\Lambda = 10$, fingers width $F = 2$ (duty cycle = 0.4). Resonant transmission through SAWs is seen at 335 MHz frequency. 1 mm long electrode fingers yield 4 times larger voltage transmission than 100 µm long fingers. (b): Electrodes period $\Lambda = 11$, fingers width $F = 3$ (duty cycle = 0.55). Resonant transmission through SAWs is seen at 313 MHz frequency. Electrodes aligned with the y axis yield twice larger response than electrodes along the z axis. The results demonstrate the anisotropy of lithium niobate.*

The first TFLN devices under test included two sets of IDTs alongside the photonic resonator waveguide, in order to compare between piezoelectric and photonic readout of a common SAWs source. Results are shown in Fig. 21. The transmission of radio-frequency voltage through the device is stronger using the piezoelectric detection, as anticipated: the peak relative transfer of voltage through piezoelectric readout was 0.02 as opposed to 0.005 with photoelastic demodulation. The peak frequencies in both transfer functions are similar, between 310-330 MHz, however the spectral details vary.

Figure 21 also shows the time domain impulse responses of both detection channels, calculated offline through the inverse Fourier transform of the measured frequency domain transfer functions. The impulse responses consist of packets of distinguishable impulses, separated by unit delay of 3.2 ns. This delay corresponds to the acoustic propagation time along one period Λ of the IDT actuator array. The impulse response of the photonic readout includes multiple such series of impulses. These represent back and forth reflections of the acoustic waves between the IDT arrays at both sides of the photonic resonator. The IDT arrays serve as partial acoustic reflectors (see Supplementary Information of [29] )

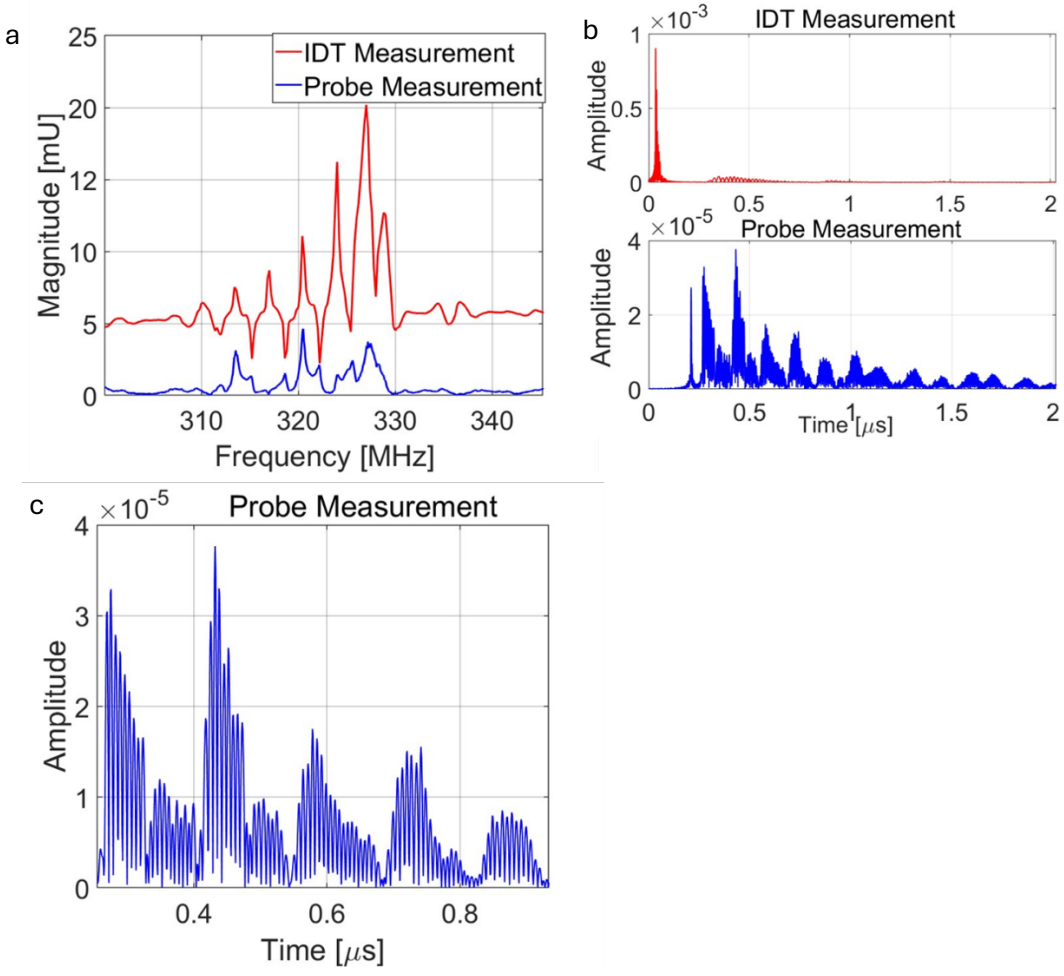


*Figure 21: Characterization of first SAW-photonic devices in thin film lithium niobate, with sending and receiving IDTs. (a) Frequency-domain transfer function of modulation voltage through piezoelectric detection*

*(red) and photonic demodulation (blue). (b) Calculated time-domain impulse responses of piezoelectric detection (top) and photonic demodulation (bottom). Multiple delayed echoes appear in the photonic output channels. (c): Magnified view of the bottom trace in panel (b). The contributions of each fingers pair in the IDT actuation are identified. Adjacent peaks are separated by 3.2 ns, corresponding to acoustic propagation over a single array period.*

In the next fabrication iteration, the receiving IDT was removed and only a single IDT remained for the piezoelectric actuation of SAWs. The frequency-domain and time-domain responses of the device are shown in Fig. 22. Unlike the earlier measurements, the output signal following photonic readout was free of multiple echoes. The temporal impulse response is dominated by two packets of impulses, separated by the acoustic propagation delay of 160 ns between the straight sections of the photonic resonator. The frequency response is characterized by single peak at 350 MHz, modulated by an interference pattern with a free spectral range of around 6.1 MHz. The results verify that the previously observed delayed echoes response was caused by acoustic reflections between the pair of IDT arrays.

The modulation depth of the output probe optical power $\frac{\Delta P}{P}$ in the experiment was 0.014. The modulation depth is related to the photoelastic perturbation magnitude $\Delta n$ according to [ref.]:

$$\frac{\Delta P}{P} = 4Q\frac{l}{L}\frac{\Delta n}{n_g} \tag{3.2}$$

Using the device parameters: $Q$ = 35000, resonator circumference $L$ = 4.64 mm, electrodes length $l$ = 1 mm, and group index $n_g$ = 2.1282, we estimate the magnitude of the photo-elastic perturbation $\Delta n$ as $1 \cdot 10^{-6}$ RIU.

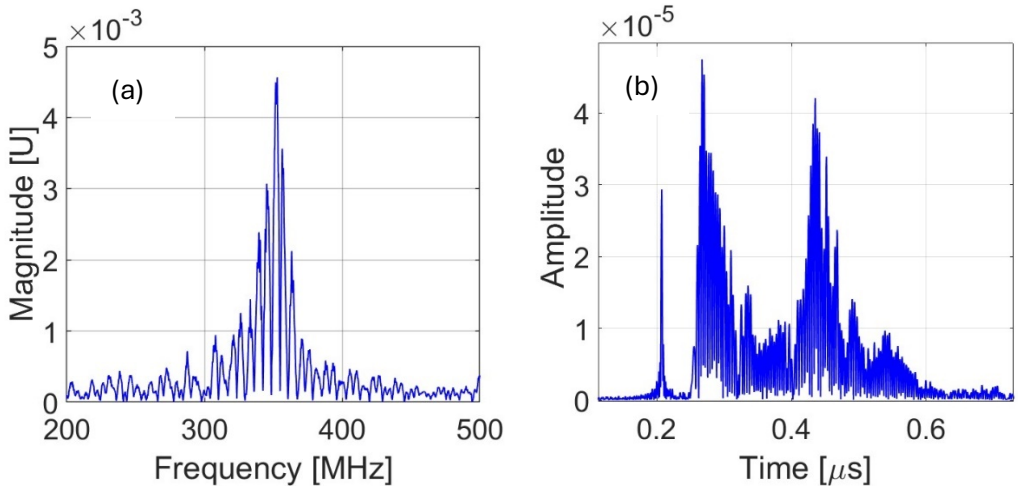


*Figure 22: Characterization of a SAW-photonic device in thin film lithium niobate, with a single IDT array for piezoelectric actuation only, and with no piezoelectric readout. (a) Frequency-domain transfer function of modulation voltage through photonic demodulation. Peak response is observed at 350 MHz. The response is modulated with a free spectral range of approximately 6 MHz. (b) Calculated time-domain impulse response. The response consists of two primary packets of impulses, corresponding to photoelastic modulation along the two straight sections of the racetrack resonator waveguide.*

In summary of this chapter, strip-loaded optical waveguides were successfully fabricated on thin-film lithium niobate, leveraging a simplified process that avoids the challenges associated with etching of $LiNbO_3$. IDTs were integrated to launch surface acoustic waves via the strong piezoelectric effect of the material, with the acoustic waves successfully read out optically through photoelastic modulation of racetrack ring resonators. The dual-IDT configuration resulted in multiple echoes due to successive acoustic reflections. These were removed in devices with a single array. The results validate the SAW-photonic platform in strip-loaded TFLN.

The response of the strip-loaded TFLN devices can be compared to other SAW-photonic devices. In previous works of the group, SAWs were launched through thermo-elastic actuation (see Chapter 1, [25], [26]). The photoelastic index perturbation $\Delta n$ in those devices was estimated as $1.2 \cdot 10^{-6}$ RIU, similar to the values we obtained for piezoelectric actuation [25]. The radio frequency of operation of the thermo-elastic devices was 2.5 GHz, 7 times higher than those of this work. The efficiency of thermo-elastic actuation scales inversely with frequency. When projected to 380 MHz frequency, the photoelastic index perturbation in the thermo-elastic SAW devices is expected to reach $1 \cdot 10^{-5}$ RIU, an order of magnitude stronger than here. However, the thermo-elastic actuation required 500 mW of optical pump power, whereas only 1 mW of radio-frequency power was applied to the IDTs of piezoelectric excitation. Altogether, the efficiency of piezoelectric actuation (in terms of $\Delta n$ per Watt) is 50 times higher than the thermo-elastic alternative. A separate study of thermo-elastic actuation of SAWs on $LiNbO_3$ reported index perturbations of $0.5 \cdot 10^{-6}$ RIU per 1 W of optical pump power [36].

SAW-photonic devices with strip-loaded waveguides in TFLN, similar to those of my work, were reported last year by the group of Prof. Xiankai Sun from the Chinese University of Hong Kong (see Chapter 1, [29]). Microwave-photonic filters centered at SAW frequencies of 0.78 GHz and 1.6 GHz were reported. The photoelastic perturbation $\Delta n$ was estimated as $4.7 \times 10^{-6}$ RIU, for radio-frequency input power of 3 mW. The actuation efficiency measured in our research is therefore consistent with their work.

The present study did not include quantitative numerical modeling of the combined piezoelectric and photoelastic response of the SAW-photonic device. Such a model would include calculations of the radio-frequency electric field profiles induced in the $LiNbO_3$ slab, the resulting forces per unit volume, and their spatial overlap with the displacement profiles of surface acoustic modes. The model would account for the tensor properties of the piezoelectric effect and the alignment of electrodes with respect to crystalline orientation. In addition, calculations would include the strain profiles associated with the acoustic modes, the

corresponding local perturbations to the dielectric tensor, and their overlap with guided light. Here too, results would depend on the polarization of the optical probe wave. The complete analysis remains for further work. Future experiments can also directly compare the piezoelectric and thermo-elastic excitations of SAWs through photoelastic detection of both in the same readout waveguide.

# 4. Surface acoustic wave devices in hybrid lithium niobate-silicon nitride platform

In this section, we report acoustic wave – photonic devices in a hybrid layer stack of lithium niobate on top of silicon nitride. Devices were fabricated by Ligentec foundry, Switzerland, according to our design. Acoustic waves are launched through the application of radio-frequency voltage to electrodes arrays on an upper piezoelectric layer of lithium niobate. The acoustic waves are monitored through photoelastic modulation of light in underlying silicon nitride photonic circuits. Preliminary results are reported below, while the complete and thorough characterization of additional devices is ongoing and extends beyond the scope of my own M.Sc. research. The results can introduce efficient acousto-optic modulation and signal processing to silicon nitride photonics.

## 4.1 Layers Stack

Figure 23 shows a schematic cross-section of the hybrid layer stack. A 300 nm thin slab of $x$-cut lithium niobate is bonded on top of the silicon dioxide cladding. A 1 μm thick aluminum layer is implemented on top of a silicon dioxide layer, 2μm above the lithium niobate slab. Arrays of electrodes of period $\Lambda$ = 18 μm are patterned in the aluminum layer, parallel to either the $\hat{\boldsymbol{y}}$ or $\hat{\boldsymbol{z}}$ axes. An additional 6 μm thick capping layer of silica was deposited on top of the lithium niobate slab. Two core layers of silicon nitride were embedded in the cladding: A main 800 nm thick layer 0.65 μm below the upper surface of the silica cladding, and an auxiliary layer of 350 nm thickness 0.1 nm below the same surface. Vertical directional couplers connect between the two layers. Light could be coupled between lensed optical fibers and inverse tapered waveguides at the main silicon nitride layer. The coupling losses were 5 dB per facet. Resonator waveguides were implemented in the main silicon nitride layer, whereas only straight waveguide sections could be realized in the upper, auxiliary layer. Part of the circuit layout is illustrated in Fig. 23(b).

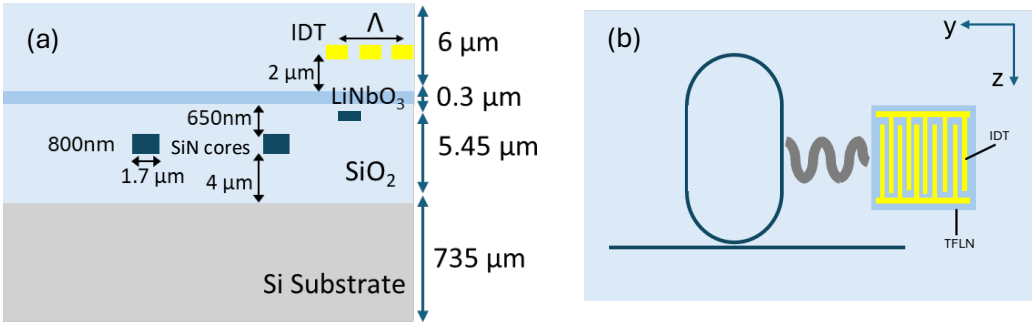


*Figure 23: (a) Illustrated cross-section of an acoustic wave – photonic device in a hybrid lithium niobate – silicon nitride layer stack (not to scale).* (b)*: Design of acoustic wave – photonic devices. Acoustic waves are launched through the application of voltage to electrodes on top of the lithium niobate layer and induce photoelastic phase modulation of probe light in waveguides in both silicon nitride layers. Phase modulation is converted to intensity reading in ring resonators.*

## 4.2 Device Layout and Geometry

The chip layout comprises two distinct sections. The upper section features ring resonators with a radius of 22.5 µm, incorporating a parameter sweep of the gap between the bus and ring waveguides, from 0.5 to 0.95 µm. IDTs were patterned parallel to straight waveguide sections along both $\hat{\boldsymbol{y}}$ and $\hat{\boldsymbol{z}}$ crystallographic directions. Two optical input ports were combined into each of the resonators by a horizontal direction coupler in the main 800 nm silicon nitride layer. The first input path remained entirely within the main layer, whereas the second one was routed up into the higher 350 nm auxiliary silicon nitride layer and back down to the main layer via two vertical directional couplers. The IDTs were aligned parallel to the waveguide segment where light propagates in the 350 nm layer. SAW-induced photoelastic phase modulation in both layers could be converted to intensity reading at the resonator output. The extent of modulation could be compared between the two optical guiding layers.

The lower section of the device contains racetrack ring resonators with bending radii of 150 µm. A coupling gap sweep ranging from 0.3 to 0.57 µm was also implemented in this section. Here, the IDTs were aligned exclusively along the $\hat{\boldsymbol{y}}$ crystallographic direction, and all waveguides were routed on the main 800 nm SiN layer. In this configuration, photoelastic phase modulation is accumulated along the two straight waveguide sections within the racetrack layout, similar to devices reported in Chapter 3 and in previous studies [25], [26]. Figure 24 presents the chip layout and a microscope image of one of the racetrack resonators.

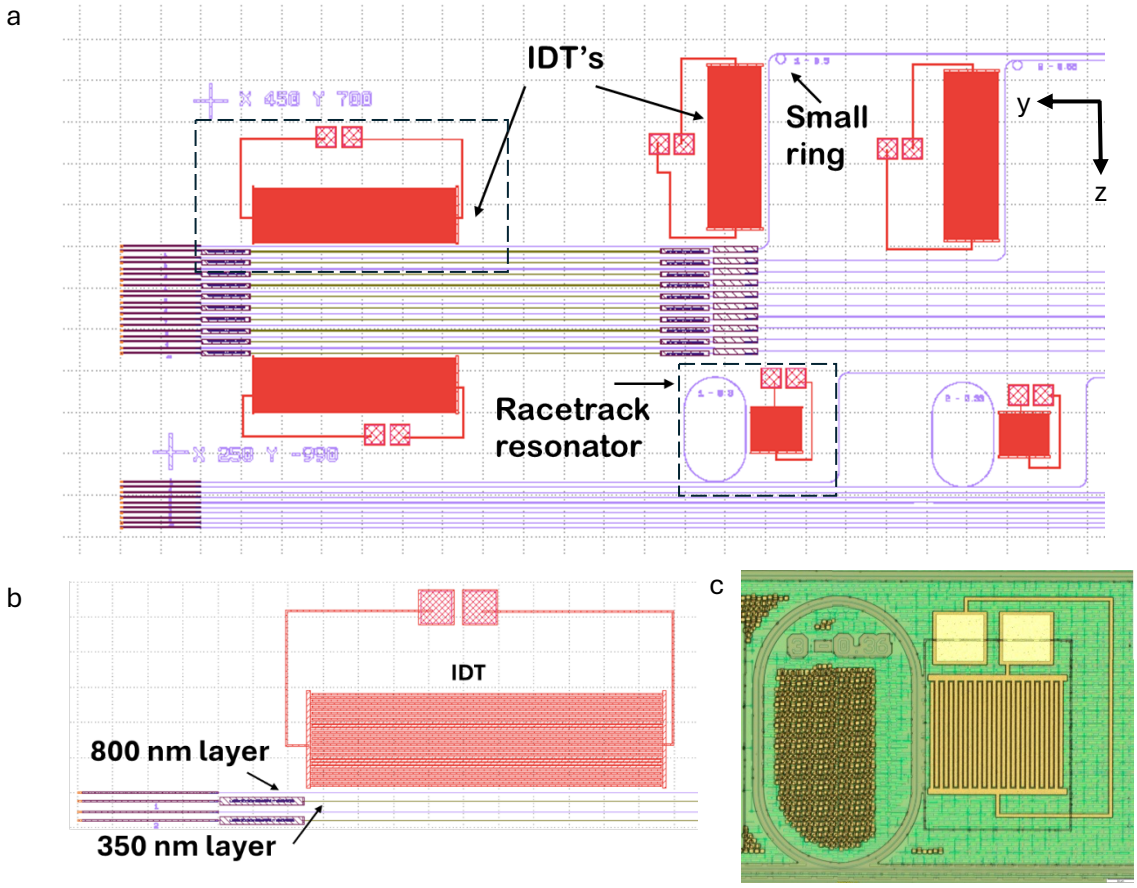


*Figure 24: (a): Part of the chip layout including SAW-photonic devices in a hybrid layers stack of lithium niobate on top of silicon nitride. The top half of the layout shows two small ring resonators. The bus waveguides leading into the resonators are routed along the $\hat{y}$ and $\hat{z}$ crystalline axes of the lithium niobate slab. Two sets of IDTs are patterned parallel to the bus waveguide. One launches SAWs along the $\hat{y}$ directions, and the other along the $\hat{z}$ axis. The bottom half of the layout consists of racetrack resonators, with adjacent IDTs in parallel with the straight waveguide sections of the resonators. In that part of the layout, the IDTs launch SAWs along the $\hat{y}$ direction. (b): Magnified view of one IDT within the upper part of the layout. Two bus waveguides run parallel with the electrodes: one strictly within the main silicon nitride core layer of 800 nm thickness, and the other is routed up towards the auxiliary 350 nm thick layer and back down towards the main layer. (c): Top-view optical microscope image of one of the racetrack resonators with the adjacent IDT.*

## 4.3 Experimental setup

The experimental setup for SAWs characterization follows the configuration described in Section 3.5. It is based on a radio-frequency vector network analyzer to supply input voltage to IDTs and monitor the photoelastic modulation of detected output probe waves. Measurements were taken at Bar-Ilan University as well as in Soreq National Research Cetner. Electrical drive signals of 0 dBm power and variable radio frequencies were applied to an IDT array under test, launching traveling SAWs via the piezoelectric effect in lithium niobate. Continuous-wave probe light at 1560 nm wavelength and 100 mW power from a tunable TOPTICA DLC laser was coupled into a straight waveguide section in the main silicon nitride core layer. The probe wavelength was tuned to the steepest spectral slope of the ring resonator transfer function, converting SAW-induced photoelastic phase modulation into intensity modulation signals. The output probe wave was amplified by an erbium-doped fiber amplifier to -7 dBm power.

The output probe wave was split in a 99:1 coupler. The 1% tap was detected in a low bandwidth photodetector, and the voltage readout provided feedback for locking the input probe wavelength to a fixed point on the spectral slope of the resonator transfer function. Locking was implemented through PID controller in a programable, multi-purpose digital Moku Pro platform (Liquid Instruments). The controller maintained the transfer of the probe optical power through the resonator at 3 dB below the off-resonance value. Light at the 99% port of the output coupler was detected by a broadband photodetector with a built-in electronic amplifier. The response of the detector was 14,400 $V \times W^{-1}$. The detected signal was electrically amplified by further 15 dB and analyzed by the VNA. The setup is illustrated in Fig. 25.

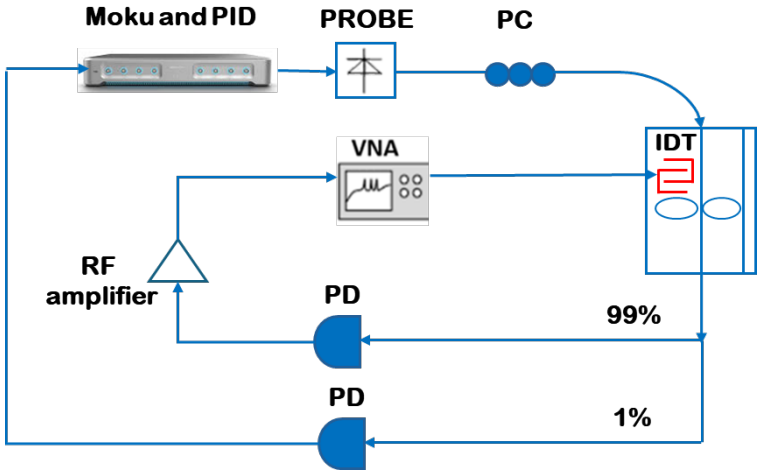


*Figure 25: Schematic illustration of the measurement setup. PC: polarization controller. PD: photo detector. VNA: vector network analyzer*

## 4.4 Experimental Results

Preliminary characterization of SAW-photonic devices through the larger racetrack resonators in the bottom half of the layout are presented below. The characterization of the entire chip, with piezoelectric actuation along both crystalline axes and photoelastic modulation in both silicon nitride layers, is still ongoing at the time of writing.

The transfer functions of optical power through the racetrack devices were measured using an optical vector network analyzer or through fine wavelength tuning of an input laser diode. Devices with 0.36 µm wide gap between the bus and ring waveguides provided transfer functions with high extinction ratios for both probe polarizations. The quality factor for the TE mode was $1.47 \cdot 10^6$, with an extinction ratio of 10.5 dB. The corresponding parameters for the TM mode were $6 \cdot 10^5$ and -7.5 dB. Results are shown in Fig. 26.

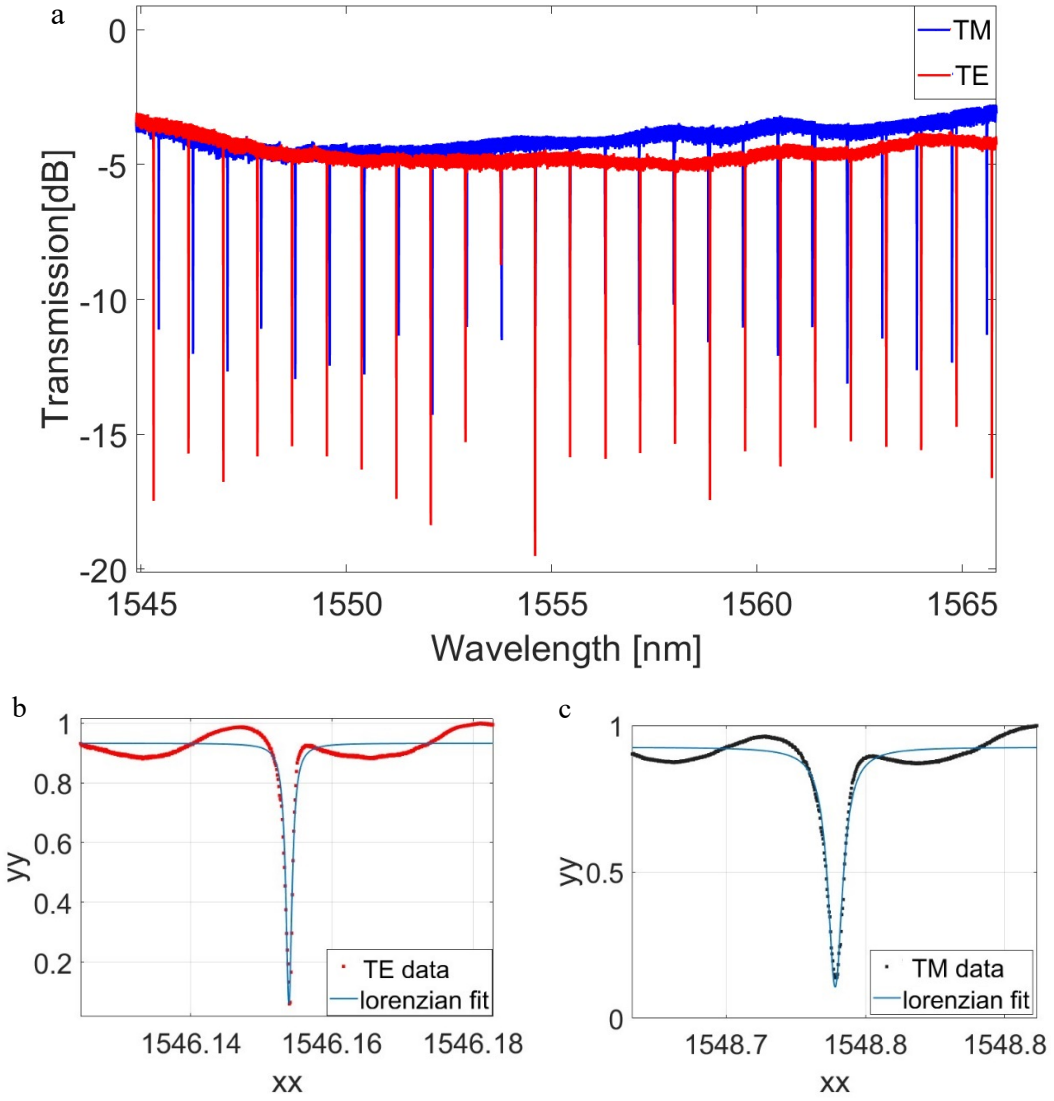


*Figure 26: (a) Measured normalized transfer functions of optical power through a racetrack resonator device, for both polarizations (see legend). (b) Magnified view of the transfer function through one resonance of the TE mode. The quality factor is 1.5 million, with an extinction ratio of 10.5 dB. (c) Magnified view of the transfer function through one resonance of the TM mode (quality factor of 600,000, extinction ratio of 7.5 dB).*

Figure 27(a) shows the normalized radio-frequency SAW-photonic transmission through the same racetrack resonator device. The normalized voltage transfer function is shown for both polarizations. The photoelastic modulation of TE polarized light is stronger by more than a factor of two. The factor matches the ratio between the quality factors of the resonator in both polarizations. The magnitude of photoelastic index modulations seen by the two optical modes are therefore similar in magnitude. Peaks are observed at acoustic frequencies of 180 MHz, 260 MHz, and 400 MHz. The frequencies are close to those of calculated acoustic modes of the devices layer stack, with a wavelength that equals the IDTs period of 18 µm (193 MHz, 292 MHz, and 429 MHz, see Fig. 27(b)).

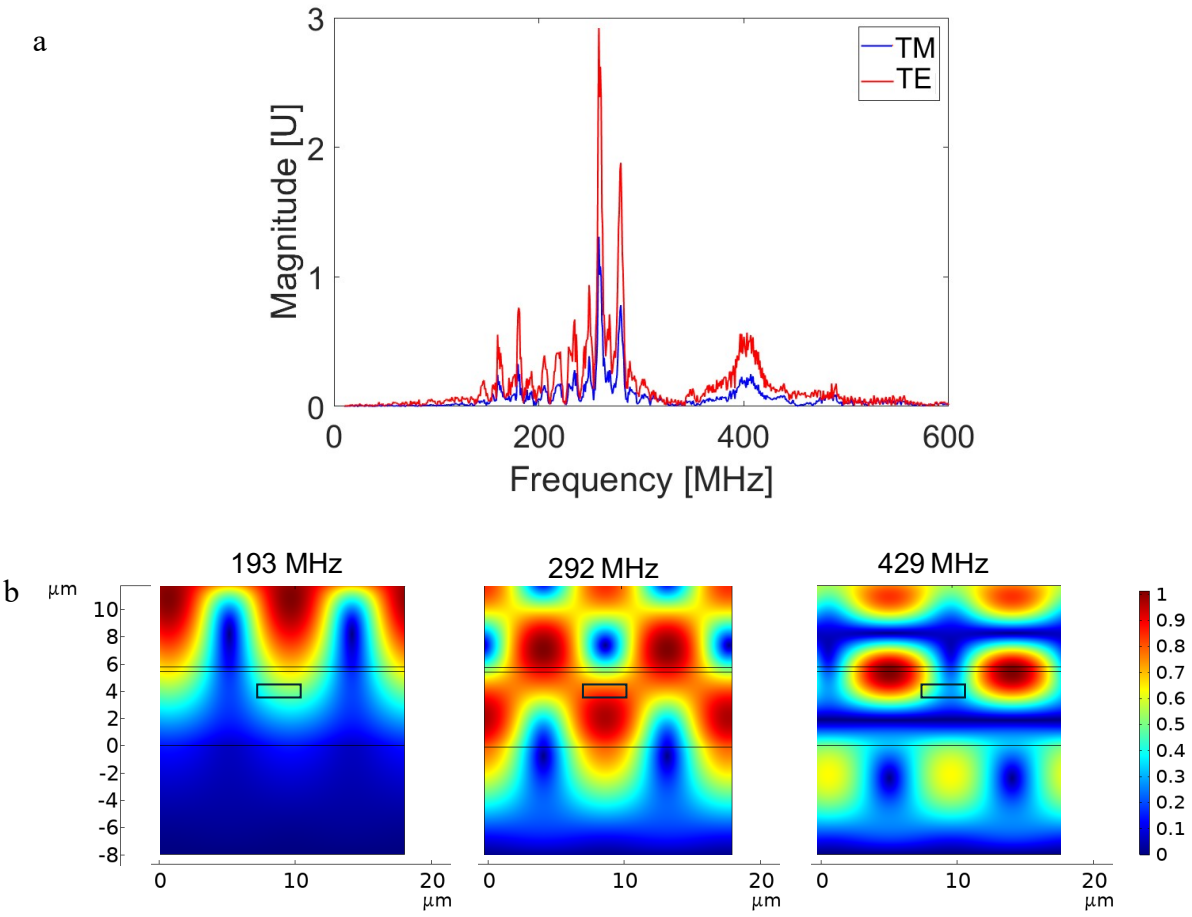


*Figure 27: (a): Measured normalized transfer functions of radio-frequency electrical power through an acoustic wave – photonic device, for both TE and TM polarizations. Peak responses are observed at 180 MHz, 260 MHz, and 400 MHz. The modulation of TM polarized light is more than twice stronger, due to the higher quality factor of the readout racetrack resonator at that polarization. (b): Calculated displacement profiles of acoustic modes in the layers stack, with a period of 18 µm. The calculated acoustic frequencies are close to those of the measured peaks.*

The modulation depth of the output probe optical power for TM polarization, (not considering radio-frequency amplification of the detected voltage), was 0.04. The racetrack resonator length was 1.38 mm, the electrodes length was 200 µm, and the group velocity of TM mode was 2 RIU. Considering the quality factor of the resonator, the magnitude of photoelastic index perturbations $\Delta n$ is estimated as $10^{-7}$ RIU (see Eq. (3.2)). The modulation is an order of magnitude weaker than the value estimated for the strip-loaded waveguide devices of Chapter 3. The difference is most likely due to the silica capping layer above the electrodes and lithium niobate slab. The silica capping restricts the mechanical displacement response to the piezoelectric forces. In the strip-loaded waveguide devices, the IDTs were patterned on a free surface of $LiNbO_3$. In future work, we will remove the silica capping layer from the hybrid devices and re-deposit IDTs on the exposed, free upper surface of the lithium niobate slab.

In summary, this chapter detailed the design, fabrication, and preliminary experimental demonstration of SAW-photonic devices on a hybrid $LiNbO_3$-over-SiN platform fabricated by Ligentec Foundry. The layer stack features a thin x-cut $LiNbO_3$ slab bonded on top of SiN core

layers embedded in silica cladding, with interdigital electrodes aligned parallel to the $\hat{\boldsymbol{y}}$ and $\hat{\boldsymbol{z}}$ crystallographic directions for SAW excitation. Devices include ring resonators for photonic readout, and they are designed to compare photoelastic modulation in two silicon nitride layers and the two polarizations of guided light. Preliminary measurements characterized the excitation of SAWs along the $\hat{\boldsymbol{y}}$ axis and their readout through TE and TM polarized light in the main, 800 nm thick silicon nitride core layer. Additional combinations are being tested in ongoing work of my group colleagues. The measurements show the excitation of three acoustic modes with 18 μm wavelength and frequencies that agree with calculations. The photoelastic modulation to the effective index of the two polarizations is similar: in the order of $10^{-7}$ RIU for 1 mW of radio-frequency power applied to the electrodes.

The SAW–photonic multi-layer devices can be compared with previous reports. As reviewed in the background section, acousto-optic modulation in thin SiN was demonstrated using a traveling-wave spiral geometry that reuses the acoustic interaction over a long interaction length of 26 cm [33]. SAWs were launched in an AlN piezoelectric layer deposited on top of foundry SiN photonics, in a manner that is compatible with commercial processes. Bonding of layers was not required. Similar to our devices, a thick upper cladding of silica was applied between the silicon nitride core and the upper piezoelectric slab, (about 4 μm), to avoid excess optical losses. Phase shifts of $\pi$ radians were achieved with the application of 9 Volts to the electrodes. Given the interaction length, the phase shift signifies $\Delta n$ of $3 \cdot 10^{-6}$ RIU: 30 times higher than in this report. At the same time, the 9 Volts applied are 40 times higher than in our case: the 0 dBm RF power used in experiments corresponds to 0.22 Volts. Although the two devices used different piezoelectric materials and different layers stacks, the efficiencies of the SAW-photonic devices appear comparable.

A separate conference paper [35] reported the feasibility of acousto-optic modulation in heterogeneous thin-film $LiNbO_3$ on SiN waveguides using wafer bonding. In that work SAWs were launched on the $LiNbO_3$ surface and detected through photoelastic perturbations to the directional coupler that forms a racetrack resonator. The results do not quantify the extent of photoelastic modulation induced and they do not address different silicon nitride layers or crystalline alignment. The work is similar to ours in the choice of layers stack and in the resonator-based readout. Here we used photoelastic perturbations to the straight waveguide sections of the resonator, rather than the coupler. That layout supports the implementation of multi-tap, delay-and-sum microwave photonic filters, as discussed in Chapter 1.

Further measurements on this platform are ongoing and will focus on quantifying SAW–optical modulation dependence versus SAW propagation direction and guided-mode polarization. These measurements will also compare the 350 nm and 800 nm SiN waveguide layers to isolate

the roles of acoustic penetration depth and photoelastic overlap in the observed modulation. The results will serve for future optimization of the devices in terms of acoustic wavelength, dimensions of silicon nitride core, and the thickness of upper and lower silica cladding layers. The effect of removing the capping layer from above the piezoelectric slab will be tested as well.

## 5. summary and Discussion

Acoustic waves have long been used for on-chip analog signal processing, mainly because they propagate slowly compared with electromagnetic waves. This slow propagation makes it possible to accumulate substantial true-time delays on a compact chip, and these delays enable narrowband radio-frequency filtering. The central motivation of this thesis was to bring these acoustic capabilities into photonic integrated circuits by using thin-film lithium niobate as a common piezoelectric layer for efficient SAW generation and acousto-optic interaction. Two implementation paths were investigated. The first used strip-loaded waveguides in TFLN, enabling a simplified in-house fabrication flow without etching of $LiNbO_3$. The second implementation path used a hybrid $LiNbO_3$ over SiN platform fabricated by Ligentec foundry, combining piezoelectric SAW actuation in lithium niobate with high-Q silicon nitride photonic readout.

Following earlier demonstrations of etch-less, strip-loaded TFLN SAW–photonic devices for microwave-photonic filtering [29], in my research I first implemented in-house fabrication that avoids dry etching of $LiNbO_3$. The devices included IDTs for piezoelectric SAW launch and strip-loaded racetrack resonators for optical probe readout through photoelastic modulation. Both piezoelectric and photonic readouts were demonstrated on the same chip, by monitoring the radio-frequency voltage transfer between a transmitting IDT and a dedicated receiving IDT in parallel with the optically detected probe modulation from the resonator. Piezoelectric detection produced stronger voltage transfer, while both channels showed similar peak frequencies in the 310–330 MHz range.

The dual-IDT geometry introduced multiple delayed echoes in the photonic impulse response due to acoustic reflections between the IDTs. These echoes were eliminated once the receiving IDT was removed. For an applied RF power of 0 dBm to the IDT, the strip-loaded TFLN devices achieved a measured probe-power modulation depth of 0.014, corresponding to an estimated photoelastic index perturbation of $\Delta n \approx 1 \cdot 10^{-6}$ RIU. The RF signal obtained following the output probe detection reached 1.12 mV. As These magnitudes indicate higher actuation efficiency than previous reports of thermo-elastic excitation of SAWs in SOI and SiN. At the same time, the index-perturbation magnitude is comparable to the earlier etch-less TFLN report.

The measurements had several limitations. The readout resonators patterned in a negative electron-beam resist were sub-optimal, with Q factor of only 35,000 and an extinction ratio of only 5 dB. The process can be much improved. For example, similar devices based on a positive resist reached quality factors of 170,000, and 14.4 dB extinction ratios. However, the use of positive resist is incompatible with the definition of ITDs. With more time, the negative resist-based process can be optimized in future work. Higher quality factors would provide deeper intensity modulation of the output probe. The devices may be extended to higher frequencies of operation, beyond 1 GHz, using shorter IDT periods.

In addition, SAWs excitation along different crystalline axes of $LiNbO_3$ in the strip-loaded devices is yet to be compared. It would also be instructive to compare thermo-elastic actuation through metallic gratings and piezoelectric actuation via IDTs side by side, with a common photonic readout resonator waveguide. Lastly, the results should be supplemented by comprehensive multi-physics modelling of the spatial distribution of thermo-elastic and piezo-elastic stresses, and their overlap with acoustic modes.

A second outcome of the work reported has been the design and preliminary experimental demonstration of SAW-photonic devices in a hybrid thin-film $LiNbO_3$ on SiN platform fabricated by the Ligentec foundry. Following an earlier conference report using a similar layers stack [35], this thesis pursued a more systematic investigation in which SAWs are launched using IDTs on the $LiNbO_3$ layer and read out optically through photoelastic modulation in SiN resonators. A key new aspect of the present work is that the hybrid chip was designed to enable controlled comparisons of SAWs directions of propagation, optical polarization, and photoelastic modulation in two SiN waveguide layers: A main buried layer that is 800 nm thick and an auxiliary upper layer of 350 nm thickness.

Only a preliminary, partial characterization has been completed thus far. The photonic readout resonators were of high quality, reaching $Q$ of 1.5 million for the TM mode and 0.6 million for TE. SAW-photonic functionality has been demonstrated at acoustic frequencies of 180 MHz, 260 MHz, and 400 MHz, in general agreement with calculations. The photoelastic index modulation was estimated as $1 \cdot 10^{-7}$ RIU. It was likely restricted by the silica capping layer above the IDTs which limited the mechanical motion of the $LiNbO_3$ slab upper surface. SAWs were launched along only one crystalline axis of the $LiNbO_3$ layer. The complete characterization of the entire set of fabricated devices still remains. Here too, future work should include a complete modelling of piezoelectric forces and strain fields, and their overlap with calculated acoustic modes. The analysis would allow for design optimization of future devices in the hybrid layers stack, in terms of core dimensions and cladding thickness. Additional sets

of electrodes can be patterned on existing devices, with shorter periods to excite higher-frequency SAWs. The capping layer will be removed for higher stimulation efficiency.

The hybrid layers stack of $LiNbO_3$ on top of SiN has been proposed primarily towards electro-optic modulation. The application of voltage to electrodes on the $LiNbO_3$ layer induces refractive index changes through the Pockels effect. Such electro-optic modulation has been the workhorse of optical fiber telecommunication for decades. Light guided in the upper SiN layer is in partial evanescent overlap with the $LiNbO_3$ slab, and it is therefore subject to electro-optic modulation [35]. The rates of electro-optic modulators routinely reach tens of GHz. However, the electro-optic modulation requires thinning down of the silica cladding layer between SiN and $LiNbO_3$, and it does not reach the main SiN layer that lies deeper in the cladding. The upper SiN layer is more lossy, and presently it cannot accommodate any circuits beyond simple, straight waveguides. In contrast, the piezoelectric modulation reported in this work reached down to the main SiN layer. This property marks a significant advantage of acousto-optic modulation over electro-optic effects in the hybrid layers stack.

In conclusion, this thesis explored SAW photonic devices based on TFLN. The work applies $LiNbO_3$ for strong piezoelectric actuation of SAWs and relies on optical reading of these waves through photoelastic modulation in high quality resonators. The results provide a path toward acousto-optic modulation and microwave-photonic signal processing on an integrated chip. The hybrid integration of $LiNbO_3$ on top of silicon-nitride, in particular, holds promise for the best of both worlds: a strong piezoelectric effect alongside high-quality and silicon-compatible passive photonic circuitry. The layer stack introduces GHz-rates modulation to the otherwise strictly passive platform of silicon nitride. I hope this investigation will assist and inspire future work, by our group and elsewhere.

# 6. References


[1] G. Keiser, “Fiber Optic Communication Networks,” in Fiber Optic Communications, Singapore: Springer Singapore, 2021, pp. 507–575. doi: 10.1007/978-981-33-4665-9_13.

[2] G. P. Agrawal, Fiber-Optic Communication Systems. Wiley, 2010. doi: 10.1002/9780470918524.

[3] R. Soref, “The Past, Present, and Future of Silicon Photonics,” IEEE Journal of Selected Topics in Quantum Electronics, vol. 12, no. 6, pp. 1678–1687, Nov. 2006, doi: 10.1109/JSTQE.2006.883151.

[4] D. Zhu et al., “Integrated photonics on thin-film lithium niobate,” Adv. Opt. Photonics, vol. 13, no. 2, p. 242, Jun. 2021, doi: 10.1364/AOP.411024.

[5] W. S. C. Chang, Ed., RF Photonic Technology in Optical Fiber Links. Cambridge University Press, 2002. doi: 10.1017/CBO9780511755729.

[6] Surface Acoustic Wave Filters. Elsevier, 2007. doi: 10.1016/B978-0-12-372537-0.X5000-6.

[7] M. H. P. Pfeiffer, J. Liu, A. S. Raja, T. Morais, B. Ghadiani, and T. J. Kippenberg, “Ultra-smooth silicon nitride waveguides based on the Damascene reflow process: fabrication and loss origins,” Optica, vol. 5, no. 7, p. 884, Jul. 2018, doi: 10.1364/OPTICA.5.000884.

[8] T. J. Kippenberg, R. Holzwarth, and S. A. Diddams, “Microresonator-Based Optical Frequency Combs,” Science (1979)., vol. 332, no. 6029, pp. 555–559, Apr. 2011, doi: 10.1126/science.1193968.

[9] A. B. Matsko and V. S. Ilchenko, “Optical resonators with whispering-gallery modes-part I: basics,” IEEE Journal of Selected Topics in Quantum Electronics, vol. 12, no. 1, pp. 3–14, Jan. 2006, doi: 10.1109/JSTQE.2005.862952.

[10] M. A. Butt, B. Janaszek, and R. Piramidowicz, “Lighting the way forward: The bright future of photonic integrated circuits,” Sensors International, vol. 6, p. 100326, 2025, doi: 10.1016/j.sintl.2025.100326.

[11] L. Chrostowski and M. Hochberg, Silicon Photonics Design. Cambridge University Press, 2015. doi: 10.1017/CBO9781316084168.

[12] Amnon. Yariv and Pochi. Yeh, Photonics : optical electronics in modern communications. Oxford University Press, 2007.

[13] M. Zhang, C. Wang, R. Cheng, A. Shams-Ansari, and M. Lončar, “Monolithic ultra-high-Q lithium niobate microring resonator,” Optica, vol. 4, no. 12, p. 1536, Dec. 2017, doi: 10.1364/OPTICA.4.001536.

[14] I. Marinković, M. Drimmer, B. Hensen, and S. Gröblacher, “Hybrid Integration of Silicon Photonic Devices on Lithium Niobate for Optomechanical Wavelength Conversion,” Nano Lett., vol. 21, no. 1, pp. 529–535, Jan. 2021, doi: 10.1021/acs.nanolett.0c03980.

[15] A. Maeder, H. Weigand, and R. Grange, “Lithium niobate on insulator from classical to quantum photonic devices,” Photoniques, no. 116, pp. 48–53, Nov. 2022, doi: 10.1051/photon/202211648.

[16] J. F. Bauters et al., “Ultra-low-loss high-aspect-ratio Si_3N_4 waveguides,” Opt. Express, vol. 19, no. 4, p. 3163, Feb. 2011, doi: 10.1364/OE.19.003163.

[17] J. F. Bauters et al., “Ultra-low-loss high-aspect-ratio Si_3N_4 waveguides,” Opt. Express, vol. 19, no. 4, p. 3163, Feb. 2011, doi: 10.1364/OE.19.003163.

[18] M. H. P. Pfeiffer, J. Liu, A. S. Raja, T. Morais, B. Ghadiani, and T. J. Kippenberg, “Ultra-smooth silicon nitride waveguides based on the Damascene reflow process: fabrication and loss origins,” Optica, vol. 5, no. 7, p. 884, Jul. 2018, doi: 10.1364/OPTICA.5.000884.

[19] R. V. Schmidt and I. P. Kaminow, “Metal-diffused optical waveguides in LiNbO3,” Appl. Phys. Lett., vol. 25, no. 8, pp. 458–460, Oct. 1974, doi: 10.1063/1.1655547.

[20] G. Poberaj, H. Hu, W. Sohler, and P. Günter, “Lithium niobate on insulator (LNOI) for micro-photonic devices,” Laser Photon. Rev., vol. 6, no. 4, pp. 488–503, Jul. 2012, doi: 10.1002/lpor.201100035.

[21] D. P. Morgan, “A HISTORY OF SURFACE ACOUSTIC WAVE DEVICES,” International Journal of High Speed Electronics and Systems, vol. 10, no. 03, pp. 553–602, Sep. 2000, doi: 10.1142/S0129156400000593.

[22] K. Hashimoto, “Surface acoustic wave (SAW) devices,” in Ultrasonic Transducers, Elsevier, 2012, pp. 331–373. doi: 10.1533/9780857096302.3.331.

[23] N. A. Ramli and A. N. Nordin, “Design and modeling of MEMS SAW resonator on Lithium Niobate,” in 2011 4th International Conference on Mechatronics (ICOM), IEEE, May 2011, pp. 1–4. doi: 10.1109/ICOM.2011.5937127.

[24] L. Shao et al., “Phononic Band Structure Engineering for High- Q Gigahertz Surface Acoustic Wave Resonators on Lithium Niobate,” Phys. Rev. Appl., vol. 12, no. 1, p. 014022, Jul. 2019, doi: 10.1103/PhysRevApplied.12.014022.

[25] M. Katzman et al., “Surface acoustic microwave photonic filters in standard silicon-on-insulator,” Optica, vol. 8, no. 5, p. 697, May 2021, doi: 10.1364/OPTICA.421050.

[26] D. Munk et al., “Surface acoustic wave photonic devices in silicon on insulator,” Nat. Commun., vol. 10, no. 1, p. 4214, Sep. 2019, doi: 10.1038/s41467-019-12157-x.

[27] D. Munk, “Integrated Silicon Photonic Filters  Using Optical and Acoustic Waves,” Bar-Ilan University, 2021.

[28] J. Capmany, B. Ortega, and D. Pastor, “A tutorial on microwave photonic filters,” Journal of Lightwave Technology, vol. 24, no. 1, pp. 201–229, Jan. 2006, doi: 10.1109/JLT.2005.860478.

[29] Y. Yu and X. Sun, “Surface Acoustic Microwave Photonic Filters on Etchless Lithium Niobate Integrated Platform,” Laser Photon. Rev., vol. 18, no. 8, Aug. 2024, doi: 10.1002/lpor.202300385.

[30] M. Churaev et al., “A heterogeneously integrated lithium niobate-on-silicon nitride photonic platform,” Nat. Commun., vol. 14, no. 1, p. 3499, Jun. 2023, doi: 10.1038/s41467-023-39047-7.

[31] L. Chang et al., “Heterogeneous integration of lithium niobate and silicon nitride waveguides for wafer-scale photonic integrated circuits on silicon,” Opt. Lett., vol. 42, no. 4, p. 803, Feb. 2017, doi: 10.1364/OL.42.000803.

[32] Z. Ruan et al., “High-Performance Electro-Optic Modulator on Silicon Nitride Platform with Heterogeneous Integration of Lithium Niobate,” Laser Photon. Rev., vol. 17, no. 4, Apr. 2023, doi: 10.1002/lpor.202200327.

[33] S. E. Kenning et al., “Broadband acousto-optic modulators on Silicon Nitride,” May 2025, doi: 10.1038/s41467-025-67618-3.

[34] W. Jin, R. G. Polcawich, P. A. Morton, and J. E. Bowers, “Phase tuning by length contraction,” Opt. Express, vol. 26, no. 3, p. 3174, Feb. 2018, doi: 10.1364/OE.26.003174.

[35] S. Ghosh, S. Yegnanarayanan, and M. Ricci, “Acousto-optic modulation in lithium niobate on silicon nitride heterogeneous waveguides,” in 2021 IEEE Photonics Conference, IPC 2021 - Proceedings, Institute of Electrical and Electronics Engineers Inc., 2021. doi: 10.1109/IPC48725.2021.9592917.

[36] Z. Zheng, H. Feng, A. T. Işık, P. J. M. van der Slot, C. Wang, and D. Marpaung, “Gigahertz thermoelastic acousto-optic modulation in lithium niobate integrated photonic device,” Nanophotonics, vol. 14, no. 26, pp. 4683–4690, Dec. 2025, doi: 10.1515/nanoph-2025-0252.

# 7. Appendix

## List of Publications

The results presented in this thesis will be submitted for journal publication later this year. In addition, part of this work has been submitted for presentation at a conference:

- M. Holsblat, I. Shafir, M. Slook, L. Dokhanian, R. Suna, S. Ben-Ami, O. Westreich, and A. Zadok, "Acousto-Optic Devices in a Hybrid Lithium-Niobate on Silicon-Nitride Layers Stack," submitted to *Conference on Lasers and Electro-Optics* (CLEO) 2026 (under review).

I also contributed to other projects that were carried out during my M.Sc. studies. These works are outside the scope of this thesis. They are presented in the following journal papers:

- I. Shafir, L. Dokhanian, M. Slook, S. Ben-Ami, M. Holsblat, O. Westreich, A. Klar, and A. Zadok," Surface acoustic wave–photonic devices in silicon nitride integrated circuits," *Applied Phys. Lett. Photonics* **10**, 096114 (2025).
- E. Layosh, E. Zehavi, A. Bernstein, M. Hen, M. Holsblat, O. Pearl, and A. Zadok, " Forward Brillouin scattering in few-mode fibers," *Light: Science & Applications* **14**, 242 (2025).
- M. Slook, S.K. Bag, L. Dokhanian, S. Ben-Ami, I. Shafir, M. Holsblat, A. Venugopalan, J. Meier, K. Mallick, T. Schneider, and A. Zadok. "Reconfigurable silicon photonic filter stage for signal processing and monitoring," *Optics Continuum* **4**, 1836–1846 (2025).

## תקציר

מעגלים פוטוניים משולבים הינם טכנולוגיה משמעותית עבור מערכות אופטיות קומפקטיות בתחומי התקשורת, החישה, המחשוב ויישומים קוונטים. מעגלים פוטוניים משולבים מאגדים יחד מוליכי גל פסיביים באיכות גבוהה, מודולטורים, גלאים ואף מקורות אור, לצורך שיפור הביצועים תוך שמירה על מימדים קטנים ויכולת יצור המוני. עם זאת, מימוש של פונקציות מסוימות במעגלים פוטוניים משולבים נותר מאתגר. לדוגמה, עיבוד אנלוגי של אותות מיקרוגל דורש השהיות זמן ארוכות, שלא ניתן לממש אותן על גבי שבב במהירות האור. גלים אקוסטיים משטחיים (SAWs) מציעים פתרון חליפי: מהירותם, הנמוכה בסדרי גודל ממהירות האור, מאפשרת צבירת השהיות משמעותיות בשטח שבב קטן. בנוסף, אינטראקציה פוטו-אלסטית עם גלים אקוסטיים יכולה לייצר אפנון בקצבי גיגה־הרץ בפלטפורמות אינטגרציה פוטוניות שהן פסיביות לחלוטין מטבען, כגון סיליקון ניטרייד. על-אף שעירור פייזו-אלקטרי הוא הדרך היעילה ביותר ליצירת גלים אקוסטיים משטחיים, הוא אינו אפשרי בפלטפורמות מרכזיות רבות של מעגלים פוטוניים משולבים, כגון סיליקון־על־גבי-מבודד, סיליקון ניטריד ועוד.

בעבודה זו הודגמה האפשרות לשלב בין עירור פייזו-אלקטרי ומעגלים פוטוניים באמצעות שכבה דקה של ליתיום ניובייט (TFLN). המחקר מתמקד בהתקנים פוטוניים מבוססי SAW המנצלים עירור פייזו-אלקטרי חזק בליתיום ניובייט לצורך מודולציה של אותות אופטיים דרך האפקט הפוטו-אלסטי. שתי גישות נבחנו עבור החיבור בין גלים אקוסטיים משטחיים לבין מעגלים פוטוניים משולבים. הגישה הראשונה עושה שימוש במוליכי גל מסוג strip-loaded על גבי TFLN ומאפשרת תהליך ייצור פשוט במיוחד ללא צורך באיכול שכבת הליתיום ניובייט. מתמרים בין־דיגיטליים (IDTs) הממוקמים על פני שטח ה- TFLN משמשים לעירור גלי קול, והקריאה הפוטונית מתבצעת באמצעות מודולציה פוטו-אלסטית של אור מולך בהתקני מהוד גל טבעתיים (racetrack resonators). תמסורת הרכיב מאופיינת בתדרי תהודה בתחום 300–400 מגה הרץ, המתאימים לאופני ההתפשטות האקוסטיים במבנה שכבות ההתקן. גודל השינוי במקדם השבירה האפקטיבי נאמד בספרה השישית אחרי הנקודה העשרונית.

קבוצת התקנים שנייה עושה שימוש באינטגרציה הטרוגנית של לוחית ליתיום ניובייט על גבי מעגל פוטוני מסיליקון ניטריד. ההתקנים תוכננו ואופיינו על ידי קבוצת המחקר שלנו, ויוצרו על ידי החברה המסחרית Ligentec בשווייץ. ההתקנים משלבים עירור פייזו-אלקטרי בשכבת הליתיום ניובייט עם מעגלים פוטוניים פסיביים באיכות גבוהה מסיליקון ניטריד. גורם האיכות של מהוד בודד הגיע ל-1.5 מיליון. מודולציה אקוסטו־אופטית במוליכי גל מסיליקון ניטרייד בעומק ההתקן הודגמה בתדר של 300 מגה הרץ. השינוי הפוטו-אלסטי במקדם השבירה בהתקנים אלה נאמד בספרה השביעית אחרי הנקודה העשרונית, עקב מגבלות שמקורן בשכבת סיליקה העוטפת את האלקטרודות המעוררות. אף על פי כן, ההתקנים ההיברידיים מאפשרים מודולציה מהירה בפלטפורמת הסיליקון ניטרייד. מחקרים עתידיים יבדקו את התלות של תגובת הרכיב בכיוון האלקטרודות ביחס לציר הגביש של ליתיום ניובייט, בקיטוב האור המולך, ובבחירה בין שתי שכבות ליבה של סיליקון ניטריד בעומקים שונים. תוצאות מחקר זה מציבות את הרכיבים האקוסטו-פוטוניים מבוססי ליתיום ניובייט כפלטפורמה מבטיחה למודולציה אקוסטו־אופטית ולעיבוד אנלוגי של אותות מיקרוגל באמצעים פוטוניים.

**עבודה זו נעשתה בהדרכתם של פרופ' אבי צדוק**

**ושל פרופסור תומר לוי**

**מן הפקולטה להנדסה של אוניברסיטת בר-אילן**

# אוניברסיטת בר-אילן

# מעגלים פוטונים פייזואלקטריים בליתיום ניובייט


## מעין הולצבלט


**עבודה זו מוגשת כחלק מהדרישות לשם קבלת תואר מוסמך בפקולטה להנדסה של אוניברסיטת בר אילן**

רמת גן תשפ"ו